RSC Advances

PAPER

View Article Online
View Journal | View Issue

Check for updates

Cite this: *RSC Adv.*, 2025, **15**, 27311

Facile, low-cost, and environment-friendly method for preparing peanut shell-based activated carbon: application to dichloromethane removal

Saeed Hassan Boroojerdi,[a] Mohsen Mir Mohammadi*[a] and Farzad Bahadoran *[b]

Received 25th February 2025
Accepted 18th June 2025

DOI: 10.1039/d5ra01361e

rsc.li/rsc-advances

Solid adsorption effectively removes hazardous air pollutants like dichloromethane (DCM), thereby mitigating serious environmental problems. In this study, activated carbon (AC) was innovatively prepared from peanut shells using a single-step physical-chemical activation technique involving CO_2 and potassium oxalate monohydrate (POM). The synthesis focused on properties, cost, and environmental impact. Optimization of AC preparation conditions employed central composite circumscribed design (CCCD) to maximize specific surface area (S_{BET}) and production yield (Y_{AC}). Two quadratic models described the relationship between synthesis variables: activation temperature ($T_{act.}$, °C), impregnation ratio (IR, g g^{-1}), and CO_2 gas flow rate (L h^{-1}) for each response. The optimized activated carbon (POMCO$_2$-AC) exhibited an S_{BET} of 1100 m^2 g^{-1} and a Y_{AC} of 21%, matching predicted values. Characterization tests indicated minimized macropores, high porosity with 83% micropore distribution, and appropriate surface chemistry. Column adsorption tests demonstrated that POMCO$_2$-AC efficiently eliminates DCM from a contaminated gas stream. Langmuir, Freundlich, and Langmuir–Freundlich models were employed for adsorption isotherm analysis. The evaluation of adsorption kinetics data was conducted using pseudo-first-order, pseudo-second-order, and intraparticle diffusion models. The results indicated that the Langmuir isotherm and pseudo-first-order models described the experimental data more accurately than other models. The maximum adsorption capacity (q_{max}) was determined to be 298 mg g^{-1} at 273 K. The adsorption mechanism was found to be governed by intraparticle diffusion in combination with the film diffusion. The study reveals that the applied preparation method effectively converts agricultural wastes, such as peanut shells, into an efficient and low-cost adsorbent for removing pollutants, making it suitable for industrial-scale air purification.

1. Introduction

Methylene chloride, also known as dichloromethane (DCM), is a chlorinated volatile organic compound that easily evaporates into the environment due to its low boiling point and high vapor pressure.[1] While not classified as a major air pollutant, it is listed as a hazardous substance by the EPA due to its potential health risks.[2–6] Additionally, some researchers highlight its negative environmental impacts.[5–9] Given the increasing use of this inexpensive chemical in industry, efforts should be made to prevent its release into the environment or to explore viable substitutes.[10]

Various methods have been developed for removing gaseous pollutants, with solid adsorption technology being one of the most effective approaches.[11] This method is cost-efficient, energy saving, and desirably efficient in pollutant removal, allowing for the recovery of both the adsorbent and the adsorbate. Other advantages include precise control and selectivity based on the adsorbent–adsorbate interactions, along with the absence of by-product generation. Solid adsorption is particularly effective in treating low-concentration pollutants.[12–14]

Engineered carbon adsorbents (ECAs) are widely used in gas purification due to their high specific surface area, porous structure, and excellent adsorption capacity. Among them, activated carbon is particularly valued for its high porosity, large surface area, and superior adsorption properties. It is a preferred adsorbent due to its favorable adsorption efficiency, affordability, chemical stability, and thermal resistance.[15–18] Traditionally, activated carbon is derived from carbon-rich materials such as coal, peat, lignite, petroleum pitch, and wood. However, due to environmental concerns, high costs, and the non-renewable nature of these sources, there is growing interest in using agricultural waste as an alternative. Biomass sources such as palm shells, fruit shells, nutshells, and coconut shells have been explored for this purpose.[19] Among them, peanut shells are a promising precursor for activated carbon production due to their abundance and compositional properties.[20]

---

[a] *Department of Environmental Engineering, Faculty of Environment, University of Tehran, Tehran, Iran. E-mail: mirmohammadi.m@ut.ac.ir*

[b] *Department of Gas Processing and Transmission Development, Research Institute of Petroleum Industry, Tehran, Iran. E-mail: bahadoranf@ripi.ir*

According to a 2023 USDA report, global peanut production reached 50.4 million metric tons across 29.5 million hectares, with China, India, Nigeria, and the USA being the largest producers.[21] Iran's peanut production in 2021 was approximately 12 200 tons from 2400 hectares.[22] Peanut waste constitutes around 25–30% of the total product weight, making it a viable feedstock for activated carbon production. Its high heating value (18.6 MJ kg^{-1}, roughly 33% of natural gas heating value) also makes it suitable for use as a biofuel.[23]

The preparation of activated carbon from biomass consists of four steps, which are briefly illustrated in Fig. 1.

The raw material undergoes dehydration and carbonization through slow heating in an oxygen-free environment, sometimes assisted by chemical agents like zinc chloride or phosphoric acid. Carbonization, a pyrolytic process, involves reactions such as dehydrogenation, condensation, hydrogen transfer, and isomerization. During this process, thermal decomposition occurs, converting biomass into primary carbon, consisting of ash, tars, and crystalline carbon. Non-carbon elements are released as gases, leaving behind solid biochar.[24,25] Some tar deposits form in the pores, which can be removed during the activation step. Activation is a crucial step that optimizes pore structure for efficient adsorption.[26] It involves the burn-off of amorphous decomposition products to increase the number and size of pores in the material.[27] Carbonization and activation are distinct processes; however, in chemical activation, they may be combined into a single-stage process for greater efficiency.[28,29] The combined activation method integrates physical and chemical activation techniques or utilizes multiple activating agents to enhance adsorption performance.[30,31]

Apart from selecting the raw material, the chosen activation method plays a crucial role in determining the overall quality of activated carbon. Here, three main factors exist for designing and manufacturing any engineered carbon (EC) adsorbent such as the activated carbon usable the industry, which are as follows:[13,14,32].

1.1 The first factor (F1) – physico–chemical properties of the adsorbent

The selection of a suitable adsorbent is particularly important for customers seeking effective adsorption performance. A high-quality adsorbent must efficiently capture the target molecule (adsorbate) while also having a long lifetime or being regenerable. Since the adsorption process depends on the properties of the adsorbent, it should possess strong adsorption capacity and favorable kinetics. Key textural and physicochemical properties, including small pore size, appropriate porosity, high micropore volume, narrow pore size distribution, and the presence of functional groups on the surface, facilitate adsorbate penetration and enhance adsorption efficiency.[15,33] For instance, Table 1 illustrates how the functional properties and textural characteristics of activated carbon derived from raw materials like peanut shells vary based on chemical activation and the use of different activating agents under various activation conditions.

As shown in Table 1, when comparing activated carbons prepared using different activation agents (H_3PO_4, $ZnCl_2$, and KOH) under identical activation conditions with a specific adsorbent (MB) during the adsorption test, potassium hydroxide (KOH) as an activation agent exhibits higher adsorption capacity (q_{max}) and surface area (S_{BET}) compared to the others (rows 2, 3, and 4).

Additionally, the textural properties of activated carbon derived from KOH significantly improve as activation conditions intensify (rows 1 and 4). Conversely, chemical activation agents such as phosphoric acid (H_3PO_4) and zinc chloride ($ZnCl_2$) require lower activation temperatures (T_{act}) than KOH to produce activated carbon with a high S_{BET} value (rows 1, 7, 8).

Although $ZnCl_2$ yields a higher S_{BET} than H_3PO_4, its usage has declined today due to environmental concerns.[19]

1.2 The second factor (F2) – adsorbent price or production cost

The production cost of adsorbents is an essential factor for both manufacturers, who aim for the most cost-effective production methods, and customers, who look for a high-quality yet reasonably priced product. Yield of activated carbon (Y_{AC}) is a key parameter in the economic evaluation of activated carbon production, as it determines the amount of activated carbon obtained per kilogram of raw material in each production cycle. Studies indicate that, regardless of the raw material chosen, the activation method and its operating conditions—along with the properties of the activated carbon—directly influence its Y_{AC}.[40–46] For example, Theydan *et al.* link the high yield of

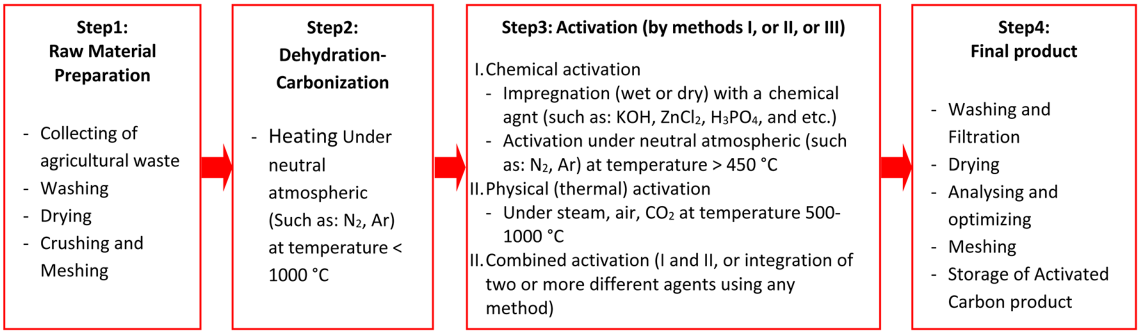

Fig. 1 Block diagram for the production of activated carbon from agricultural waste biomass precursors.

Table 1 Comparison of the functional properties and textural characteristics of activated carbon prepared from peanut shell with different chemical activators

		Activation condition			Textural properties of AC					
No.	Activator	IR (g g^{-1})	T_{act} (°C)	t_{act} (h)	S_{BET} (m^2 g^{-1})	V_t (cm^3 g^{-1})	V_{micro} (cm^3 g^{-1})	Adsorbate	q_{max} (mg.g^{-1})	Ref.
1	KOH	6.6	750	2	1523.2	0.7	0.5	H_2S	97.6	34
2	H_3PO_4	1	550	1	56.8	—	—	MB	270.2	35
3	$ZnCl_2$	1	550	1	512.2	—	—	MB	291.2	35
4	KOH	1	550	1	691.7	—	—	MB	332.2	35
5	$ZnCl_2$	1.8	650	0.3	1200	—	—	Iodine/MB	1114/238	36
6	$ZnCl_2$	5	480[a]	1.5	1025	—	—	EB/T/p-X	339.7/424.5/318.5	37
7	$ZnCl_2$	5	480[a]	1.5	1642.7	0.4	—	MB	876.4	38
8	H_3PO_4	5	450	3	1138.0	0.7	0.4	dye	31	39

[a] Carbonization by heating from 25 °C to 200 °C for 30 min and then at 480 °C for another 90 min, under a nitrogen flow **IR: impregnation ratio, T_{act}: activation temperature, t_{act}: activation time, S_{BET}: Brunauer, Emmett and Teller surface area, V_t: total pore volume, V_{micro}: micro pore volume, q_{max}: maximum adsorption capacity, MB: methylene blue, EB: ethyl benzene, T: toluene, p-X: p-xylene.

activated carbon (47.1%, calculated based on the weight of raw material) from date pits to the role of the chemical activation agent ($FeCl_3$) in enhancing micropore content.[42] Wang and colleagues found that increasing activation conditions (temperature from 850 to 900 °C, duration time from 3 to 3.5 hours) improved S_{BET} (774 to 1980 m^2 g^{-1}) but reduced Y_{AC} (80.5% to 9.6%, calculated based on the weight of carbonized raw material). In contrast, chemical activation using KOH (IR of 4 g g^{-1}) required less time (1 hour) to achieve nearly the same S_{BET} (1976 m^2 g^{-1}). Raising IR (2 to 8 g g^{-1}) increased surface area (1310 to 2037 m^2 g^{-1}) but lowered yield (87.9% to 35.8%, calculated based on the weight of carbonized raw material).[41]

1.3 The third factor (F3) – ecological environmental impact during production or use of adsorbent

This factor refers to the environmental impact associated with the production and use of an adsorbent. Minimizing environmental impact is crucial in adsorbent production. Despite its effectiveness, chemical activation has drawbacks, including extensive washing requirements to remove residual activating agents, which result in toxic wastewater and increased costs.[16] Studies indicate that alkaline activating agents—such as potassium carbonate (K_2CO_3)—are preferred over $ZnCl_2$ and H_3PO_4 due to their lower energy consumption and reduced environmental impact.[47] Research by Tay *et al.* demonstrates that K_2CO_3 is more effective than KOH in producing activated carbon with high porosity and yield. Additionally, K_2CO_3 is nearly 100% recoverable during activation and is a non-toxic compound, commonly used in food additives.[40,47] Potassium oxalate (PO) has been introduced as an alternative alkaline activator, similar to K_2CO_3, for preparing activated carbon from biomass.[19] Early experiments show that PO produces activated carbon with desirable properties (F1), good yield (F2), and high chemical recovery rate (F3) while not requiring severe activation conditions (impregnation ratio (IR), activation temperature (T_{act}), and activation time (t_{act})) (F2 and F3).[48] These advantages, along with its non-toxic nature, make PO an environmentally and economically (F3) preferable option over KOH. The formation and development of porosity during activation using PO are attributed to the reduction of the activating agent and the formation of K, K_2O, CO_2, and CO.[49–52] Findings indicate that excess PO and residual metallic potassium on the carbon surface during activation can block pores, leading to a significant decrease in accessible surface area, reduced production yield, and increased burn-off of the carbon precursor.[50–52] Instead of increasing the weight ratio of the chemical activator to the carbonous precursor (IR), integrating CO_2-assisted activation further improves the structural properties of the adsorbent while lowering greenhouse gas emissions.[30,31]

This research focuses on fabricating cost-effective activated carbon (F2) with suitable physicochemical properties (F1) for dichloromethane (DCM) adsorption from polluted gas streams while reducing environmental impact (F3). Peanut shells from Pars Abad, Ardabil, Iran, were chosen as carbon precursors due to their high volatile, carbon content and low ash content. The study employs a single-step combined activation process with CO_2 and potassium oxalate monohydrate (POM), optimized using the central composite constraint design (CCCD) method, a subset of response surface methodology (RSM).[53]

This study optimized the preparation conditions for activated carbon (AC), including impregnation ratio (IR, (g g^{-1})), activation temperature (T_{act}, (°C)), and CO_2 gas flow rate (L h^{-1}), with AC yield (Y_{AC}, (%)) and specific surface area (S_{BET}, (m^2 g^{-1})) as targeted responses. To date, the preparation of AC from peanut shells (PS) using this activation technique has not been reported. Therefore, the textural and chemical characterizations of the optimal activated carbon (POMCO_2-AC) were conducted using CHNSO analysis, N_2 adsorption–desorption isotherms, FTIR, SEM, and pH_{pzc} tests. Adsorption tests in a fixed-bed column were conducted to compare POMCO_2-AC's performance with commercial AC for dichloromethane (DCM) removal. Adsorption isotherms, including Langmuir (two parameters), Freundlich (two parameters), and Langmuir–Freundlich (three parameters) models, were used to analyze adsorption behavior, essential for optimizing pollutant removal and adsorption system design.[54–56] Beyond AC production and equilibrium studies, three additional objectives were pursued: (1) applying kinetic models to understand adsorption rate and mechanism, (2) evaluating adsorbent stability through regeneration and reuse, and (3) assessing the economic viability of the synthesized adsorbent compared to commercial alternatives.

This research demonstrates the value of converting agricultural waste into a cost-effective and efficient adsorbent for air purification, with a focus on indoor air pollutant removal.

2. Materials and methods

2.1 Materials

Waste peanut shells were sourced from Parsabad, Ardabil province, Iran. They were initially washed several times with tap water and then thoroughly cleaned using an ultrasonic washer for one hour. The washed shells were oven-dried at 110 °C for 24 h, then crushed and sieved using U.S. standard mesh sizes 6 and 10. The Potassium oxalate monohydrate (RPE – For analysis) was supplied by Carlo Erba. Other chemicals used in this study were of analytical reagent grade and provided by Merck Company. For gas-phase adsorption experiments, a main gas cylinder containing nitrogen gas with dichloromethane at a concentration of 3000 ppm was used as the feed gas.

2.2 Activated carbon preparation

Activated carbon was produced through carbonization and simultaneous combined chemical and physical activation in a single-step process, as follows:

Initially, 5 grams of peanut shells were mixed with a 3 M solution of potassium oxalate monohydrate in a mass ratio defined by the experimental design (IR ranging from 0 to 2 (g g^{-1})) at 60 °C for 2 hours. The impregnated sample was then dried in an oven at 110 °C under atmospheric pressure for 24 hours. The dried sample was loaded into a stainless-steel reactor with a nominal diameter of 2 inches, which was placed inside a muffle furnace. The reactor was equipped with gas inlet and outlet ports. At this stage, inert nitrogen (N_2) gas was introduced into the reactor under atmospheric conditions, and the furnace temperature was increased in two steps. First, the furnace was heated from room temperature to 200 °C and maintained for 1 hour. Then, the temperature was raised at a controlled rate to the activation temperature, as defined by the experimental design (650–850 °C). At this point, CO_2 gas flow (ranging from 0 to 9 L h^{-1}, based on the experimental design) replaced the N_2 gas, and the reactor was maintained under these conditions 30 minutes. After this period, the furnace was cooled to room temperature according to a pre-defined program. Following carbonization and activation, the cooled product was removed from the reactor, washed with 1 M hydrochloric acid and distilled water, and filtered. The filterated product was then dried in an oven at 110 °C for 24 hours and sieved. The activated carbon synthesized under optimal conditions (IR, T_{act}, and CO_2 gas flow rate) was designated as POMCO_2-AC.

2.3 RSM-FRCCCD experimental design

Response surface methodology (RSM) is a set of mathematical and statistical techniques used in experimental design to optimize an objective function while minimizing cost and time. Instead of conducting numerous experiments to find the optimal response, RSM employs reduced and simplified experimental designs to gain a precise understanding of the system and determine the optimal operational parameters.[57] In this study, the full rotatable central composite circumscribed design (FRCCCD) with resolution V and three independent variables was used to analyze the response patterns and identify the optimal combination for synthesizing activated carbon from peanut shells.[58] One key advantage of this method is its ability to minimize the effects of extraneous uncontrolled factors by randomizing the order of experiments. The central composite design (CCD) was structured with three independent variables: (X_1) the mass ratio of potassium oxalate to peanut shells (impregnation ratio, IR in g g^{-1}), (X_2) activation temperature (T_{act}, in °C), and (X_3) CO_2 gas flow rate (in L h^{-1}), each tested at five different levels. These levels were determined with coded values of −1 (minimum), 0 (medium), +1 (maximum), $-\alpha$, and $+\alpha$. Alpha (α) represents the distance from the center point, calculated as $2^{n/4}$, and may fall within or beyond the range.[59] The actual and coded levels of the independent variables are presented in Table 2.

In this study, design-expert software (version 12) was used for both experiment design and result analysis. The response variables selected were Y_1, the surface area of synthesized activated carbon (S_{BET}, m^2 g^{-1}), and Y_2, the activated carbon production yield (YAC, %). In the central composite design (CCD) method, the number of experiments is determined by the following equation:[60]

$$\text{Run} = 2^n + (2n + 1) + r \tag{1}$$

where n represents the number of independent factors and r denotes the number of experiment repetitions.

The analysis of experimental data, along with the generation of response surfaces and contour plots, is conducted using the response surface regression method within the statistical analysis system of design-expert software. A second-order polynomial model was used to fit the experimental data and obtain the regression coefficients. The general second-order polynomial model used in response surface analysis is as follows:[60,61]

$$y = \beta_0 + \sum_{i=1}^{k} \beta_i x_i + \sum_{i=1}^{k} \beta_{ii} {x_i}^2 + \sum \sum_{i<j=2}^{k} \beta_{ij} x_i x_j + \varepsilon \tag{2}$$

Table 2 Levels of independent variables and experimental range

		Coded range				
Independent variable	Notation	$-\alpha(-1.68)$	−1	0	+1	$+\alpha(-1.68)$
IR (g g^{-1})	X_1	0	0.4	0.9	1.5	1.2
T_{act} (°C)	X_2	666	700	750	800	834
CO_2 rate (L h^{-1})	X_3	0	1.8	4.4	7	8.8

The second-order model that contain close to (but not less than) ρ design points where:

$$\overbrace{\rho = 1 + \underbrace{2k}_{\text{(k) Linear terms + (k) quadratic terms depending on each of the three factors}} + \underbrace{\frac{k(k-1)}{2}}_{\text{Interaction terms between the factors}}}^{\text{Intercept or average}}, \quad \text{For example: } \rho = 1 + (3+3) + 3 \tag{3}$$

In eqn (3), ρ represents the number of terms in the second-order model, while 1 indicats intercept, first k denotes the number of first-order terms, second k represents the number of pure quadratic terms, and $k(k-1)/2$ accounts for the number of interaction terms. In other words, given k value of 3 (three independent factors), the regression model contains 10 terms, which include one intercept (or the average of data), three coefficients for main effects (linear terms), three coefficients for pure quadratic main effects and three coefficients for two factor interaction effects. In the equation above, y is the response variable, β_0 is the constant coefficient, β_i, β_{ii} and β_{ij} are the coefficients for the linear, quadratic and interaction effects, X_i and X_j are the factors and ε is the error.

2.4 Analytical methods and apparatus

The characteristics of peanut shell and prepared activated carbon were determined as follows:

- A CHNS–O elemental analyzer (Vario max-elementar) was used to determine the C, H, N and S element contents.
- A proximate analysis was conducted to determine the volatile matter, moisture, and ash content, following the standards ASTM D3175, D3173, and E1755. The fixed carbon content was calculated by difference.
- The BET (Brunauer–Emmett–Teller) surface area of the activated carbons was also determined by measuring the nitrogen adsorption at 77 K using a Micromeritics ASAP 3020 automated system. The samples were degassed at 200 °C for minimum 3 h under the neutral gas flow prior to the measurement. Additionally, the pore size distribution of activated carbons was determined using the BJH (Barrett–Joyner–Halenda) methodology.
- The functional groups on the surface of PAC before adsorption experiment were identified with Fourier Transform Infrared (FTIR) spectrophotometer (ALPHA-BRUKER).
- The field emission scanning electron microscopy (FE-SEM ZEISS Sigma 300) was used to achieve the morphological structure of the peanut shell and activated carbon.
- GC analyzer (MODEL: CP-3800, Varian) equipped with a flame ionization detector (GC/FID), for analysing gas mixture.
- GC (MODEL: CP-3800, Varian) equipped with a thermal conductivity detector (GC/TCD), for real-time monitoring and recording of BTCs.
- Mass flow controllers (MFCs), suitable for any gas (Model: Brooks), for controlling and adjusting gas flow.

2.5 Adsorption experiment

The research examined adsorption capacity, stability test, equilibrium isotherms, and adsorption kinetics using two different adsorption modes: (1) dynamic (fixed-bed column) adsorption mode as shown in Fig. 2 and (2) static (volumetric) mode. Dynamic adsorption system consists of three main components:

1 - Gas feeding package section: includes main gas cylinders containing DCM (1000, 2000, and 3000 ppmv) and a pure nitrogen gas cylinder. It is equipped with pressure regulators, mass flow controllers (MFC) for each cylinder, readout and controller system (RCS), and a static mixer for diluting the feed gas at different DCM concentrations (C): $C < 1000$ ppmv, 2000 ppmv $< C <$ 3000 ppmv, $C <$ 3000 ppmv. This section also includes a helium gas cylinder, which is used to determine the dead volume occupied by the adsorbent in the column. 2 – Adsorption section: 2.1 A jacketed pyrex column with a double

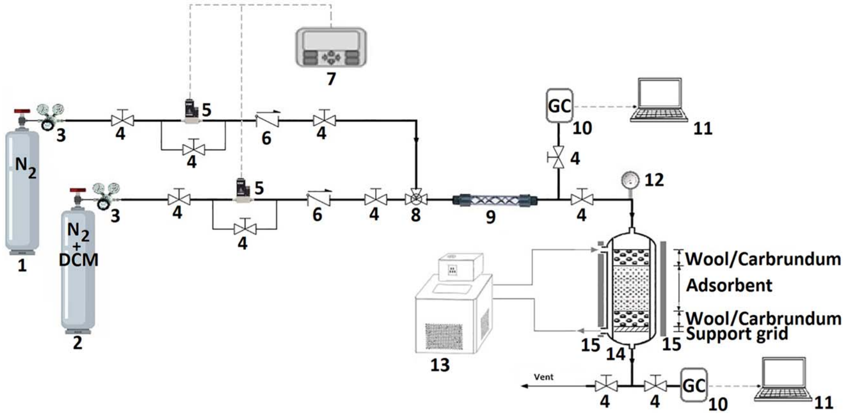

Fig. 2 Schematic setup of the adsorption experiment: (1) N_2 gas cylinder; (2) main gas (N_2 – DCM mixed gas) cylinder; (3) pressure regulator; (4) valve; (5) mass flow controller; (6) check valve; (7) readout and controller system-RCS; (8) 3-way valve; (9) static mixer; (10) gas chromatography; (11) computer; (12) digital pressure gage; (13) digital circulated (cold/hot) water bath; (14) adsorption column; (15) heating jacket (all of the equipment is among the best available on the market, offering a high degree of accuracy).

wall (40 cm length, 0.5 cm inner diameter). 2.2 A digital Wise-Circu circulation water bath for column temperature control. 2.3 An electric strip heater with a dimmer for column heating, used for degassing and adsorbent activation before experiments. 3 – Gas chromatography (GC) section: 3.1 an offline GC analyzer (MODEL: CP-3800, Varian) equipped with a flame ionization detector (GC/FID) for measuring the DCM concentration in the column inlet feed and outlet stream. 3.2 An online GC (MODEL: CP-3800, Varian) equipped with a thermal conductivity detector (GC/TCD) for real-time monitoring of dynamic adsorption and breakthrough curve recording. The GC/TCD instrument has been structurally and software-modified to route gas effluent directly to the GC detector, enabling moment-to-moment measurement of DCM concentration in millivolts (or microvolts) (used only in dynamic mode).

The experiments were conducted according to the following steps: 1 – system preparation step: before loading the adsorption column, the gas flow rate is set to 22 mL min^{-1}, and the DCM concentration in the feed gas is adjusted based on the study requirements using MFCs. DCM concentration in the feed gas verified using the offline GC (GC/FID) device. The column, containing an adsorbent (length of the adsorbent bed 3 cm), is loaded according to Fig. 2. The system is purged with nitrogen gas and checked for leaks. The adsorption column is degassed, and the adsorbent is activated at 200 °C for 2 hours. At this point, the system is ready to proceed with the experiments. 2 – Adsorption tests: before placing the loaded column into the system, the peak concentration of the feed gas is observed and recorded using an online GC (GC/TCD) device, based on the voltage difference between pure nitrogen gas and feed gas. After completing the preparation step (step 1), the feed gas replaces nitrogen gas. Adsorption begins as soon as the feed gas enters the column, and the outlet stream is continuously monitored using the online GC device, which records the breackthrough curve in real time. In addition, the gas concentration in the outlet stream at different times is analyzed using the offline GC (GC/FID) device to enhance the accuracy of adsorption capacity calculations. The equilibrium adsorption capacity was calculated in mg g^{-1} using the following equation:[62]

$$q_t = \frac{F}{m}\int_0^{t_t}(C_0 - C)\mathrm{d}t \tag{4}$$

where F is the feed gas flow rate in L h^{-1}, m is the amount of adsorbent in g, C_0 and C represent the concentrations of DCM in the gas phase at the inlet and outlet of the adsorber, respectively in mg L^{-1}. The parameter t_t corresponds to the time equivalent to the total or stoichiometric capacity in hours (h). In the adsorption process, $q_t = q_e$ is achieved when the equilibrium time (t_e) is reached, indicating the adsorption capacity at equilibrium.

With minor modifications, the dynamic adsorption system can be adapted for static studies under batch conditions. These modifications include installing a regulating valve at the inlet of the adsorption column for precise gas pressure control, using a pressure transmitter (PT) along with a personal computer (PC) for monitoring and recording pressure variations until equilibrium is reached. Additionally, the column outlet valves must remain closed during operation.

The static adsorption process involves evacuating the system using a vacuum pump before introducing DCM gas, followed by a gradual pressure reduction upon opening the adsorption vessel valve until equilibrium pressure is achieved. During adsorption, gas pressure is continuously measured and transmitted to a PC for data recording. At equilibrium, the gas concentration is determined using an offline GC/FID device.

3. Results and discussion

3.1 Characterization of activated carbon

The results of the proximate and elemental analysis of the peanut shell and POMCO$_2$-AC, along with some physical characteristics of biochar and ACs prepared in this study, are summarized in Table 3.

As shown in Table 3, peanut shells, with high volatile and carbon content and low ash content, are considered excellent precursors for AC conversion. Following carbonization and activation processes, the carbon content demonstrated an upward trend, increasing from 55.7% in peanut shells to 91.9% in POMCO$_2$-AC. Meanwhile, the fixed carbon (FC) content increased significantly, rising from 27.5% in the original peanut shells to 89.6% in POMCO$_2$-AC. Additionally, the volatile

Table 3 Characteristics of the biochar (BC) and activated carbons (ACs) from peanut shell

		Bio-char (BC) and types of activated carbons			
	PS	BC[a]	POM-AC1[b]	POM-AC2[c]	POMCO$_2$-AC[d]
Elemental analysis (dry basis, wt%)					
C	55.7	—			91.9
H	6.3	—			0.5
N	0.7	—			<0.1
S	<0.01	—			—
O	36.4	—			3.4
Proximate analysis (wt%)					
Moisture	1.9				2.5
Volatile matter	69.7				3.8
Fixed carbon	27.5				89.6
Ash	0.9				4.1
Typical properties					
S_{BET}[e] (m^2 g^{-1})	—	1.3	76.6	601.4	1100.0
V_t[f] (cm^3 g^{-1})	—	0.004	0.012	0.284	0.545
V_{micro}[g] (cm^3 g^{-1})	—	0.004	0.006	0.242	0.450
V_{meso}[h] (cm^3 g^{-1})	—	0.000	—	0.042	0.095
d_{ap}[i] (Å)	—	113.01	—	18.91	18.87

[a] Without activation under operating condition ($T_{\mathrm{carbonization}} = 400$ °C, $t_{\mathrm{carbonization}} = 1$ h). [b] (POM) chemical activation under operating condition (IR = 1 g g^{-1}, $T_{\mathrm{act}} = 550$ °C, $t_{\mathrm{act}} = 0.5$ h). [c] (POM) chemical activation under operating condition (IR = 2 g g^{-1}, $T_{\mathrm{act}} = 700$ °C, $t_{\mathrm{act}} = 0.5$ h). [d] (CO$_2$) physico-(POM) chemical hybrid activation under optimal operating condition (IR = 1 g g^{-1}, CO$_2$ rate = 4 L h^{-1}, $T_{\mathrm{act}} = 750$ °C, $t_{\mathrm{act}} = 0.5$ h). [e] BET (Brunauer–Emmett–Teller) surface area. [f] Total pore volume. [g] Micropore volume. [h] Mesopore volume. [i] Average pore width.

compound (VCM) content underwent a significant reduction, decreasing from 69.7% in peanut shells to 3.76% in the produced activated carbon ($POMCO_2$-AC). These changes are attributed to the decomposition of hemicellulose and cellulose during processing.[34] The ash content in activated carbon is a critical factor; high ash levels reduce mechanical strength and adsorption capacity, making it unsuitable for commercial use.[63] Table 3 shows that the produced activated carbon ($POMCO_2$-AC) has minimal ash content compared to other studies. This is due to efficient thermal decomposition, washing, and filtration processes, as well as the natural plant origin of peanut shells.[34,63,64] Moreover, a significant reduction in oxygen content is observed (from 36.4% in biomass to 3.4% in activated carbon), attributed to major dehydration (removal of hydroxyl groups, OH–) and partial decarboxylation (removal of carboxyl groups, COOH–) during carbonization and activation processes.[34]

BET analysis reveals that biochar prepared at 400 °C without chemical activation has a significantly lower specific surface area (S_{BET}) compared to activated carbons. This indicates that activation conditions, such as activation temperature and activating agents, significantly influence SBET and porosity characteristics; higher temperatures (400 °C to 750 °C) enhance S_{BET}. $POMCO_2$-AC, produced using combined chemical activation with $K_2C_2O_4$ and physical activation with CO_2, demonstrates a superior specific surface area compared to POM-ACs produced with only chemical activation—even with higher concentrations of activating agents. The combined method also increases micropore volume. Commercial activated carbons typically have S_{BET} values ranging from 500 to 2000 $m^2\ g^{-1}$, and $POMCO_2$-AC meets this criterion.[65,66] Its production from low-cost, renewable peanut shells using environmentally friendly chemical agents in minimal quantities and moderate activation temperatures is notable for technical, economic, and environmental reasons.

Fig. 3 and 4 compare the N_2 adsorption–desorption isotherms and BJH (Barrett–Joyner–Halenda) pore size distribution for the activated carbons produced from peanut shells using different activation methods (a, b, c) as follows:

(a) $POMCO_2$-AC, combined physical–chemical activation using CO_2 & POM under operational conditions.

($T_{act} = 750$ °C, CO_2 RATE $= 4\ L\ h^{-1}$, IR $= 1\ g\ g^{-1}$, $t_{act} = 0.5$ h)

(b) CO_2-AC, only physical activation using CO_2 under operational conditions.

($T_{act} = 750$ °C, CO_2 RATE $= 4\ L\ h^{-1}$, $t_{act} = 0.5$ h)

(c) POM-AC, only chemical activation using POM under operational conditions.

($T_{act} = 750$ °C, IR $= 1\ g\ g^{-1}$, $t_{act} = 0.5$ h)

According to Fig. 3: (a) All AC curves exhibit IUPAC type-I isotherms. (b) A less rounded knee in curves 3a and 3b (zone 1) indicates a narrower distribution of micropores (less than 2 nanometers) at very low relative pressure ($P/P_0 < 0.02$). This observation is confirmed by the pore size distribution results presented in Fig. 4. In other words, although all ACs demonstrate significant porosity within the diameter range of less than 2 to 150 nanometers, the combined methodology results in the preparation of carbons with an even narrower and more homogeneous pore size distribution, as well as minimal macropore presence compared to those obtained through other activation methodologies. (c) The lower slope in the linear portion of curves 3a and 3c (zone 2), along with the presence of a smaller hysteresis loop (if any) at a P/P_0 range of 0.3–0.9, suggests a lower mesopore content (ranging from 2 to 25 nanometers).

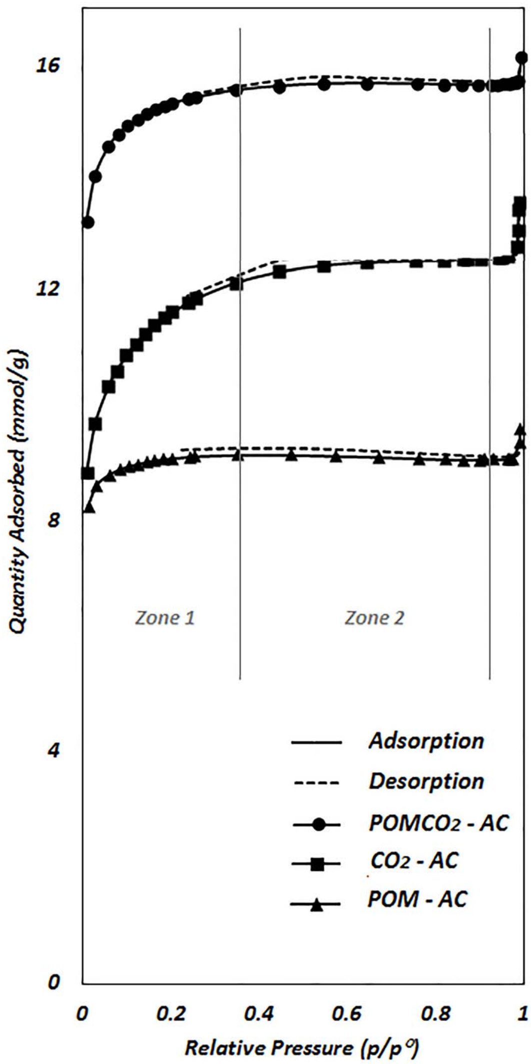

Fig. 3 N_2 adsorption (filled symbols) and desorption (open symbols) isotherms at 77 K for the $POMCO_2$-AC (●), CO_2-AC (■), POM-AC (▲).

These findings can be interpreted as follows:

In the present study, the simultaneous processes of carbonization and activation lead to pore creation, development, enlargement, and structural reorganization. As the reactor temperature rises to 750 °C, triggering pyrolytic reactions, the structure of the carbon precursor impregnated with the chemical activating agent POM breaks down, typically forming bent aromatic sheets or strips, which may generate gaps between them. Researchers suggest that without the presence of the chemical agent during this process, the carbonized sample would likely exhibit a highly disordered structure.[30] However, with the chemical activating agent

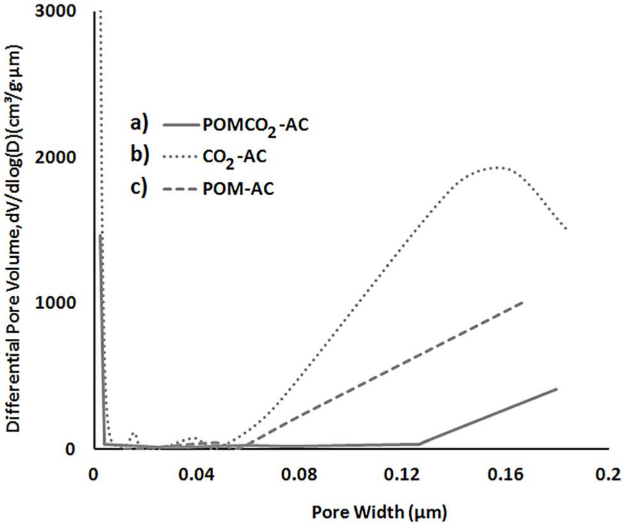

Fig. 4 BJH pore size distribution for the (a) POMCO$_2$-AC, (b) CO$_2$-AC, (c) POM-AC.

present, chemical interactions and gas production facilitate gas diffusion through these gaps, contributing to pore formation. The development of the pore structure is further enhanced during physical activation with CO$_2$. Simultaneously, structural reorganization leads to partial closure of the gaps, forming a homogeneous pore structure with a highly narrow pore size distribution.

To further investigation the impact of the activation process on pore and cavity formation on the surface of activated carbon, scanning electron microscope (SEM) images were taken of peanut shells and POMCO$_2$-AC. These images were used to examine possible changes in the morphological features of the samples before and after activation. The analysis results are presented in Fig. 5.

By comparing the SEM images of the peanut shell and POMCO$_2$-AC activated carbon, it is evident that the surface of the raw peanut shell (left image) is smooth and non-porous, exhibiting a dense fibrous structure. However, following the carbonization and activation of the PS sample (right image), it develops a well-structured, uniform surface with an organized microporous structure and accompanying cavities.[48,58–61] Researchers such as Prachner and colleagues suggest that, in addition to chemical activation, physical activation with CO$_2$ enhances pore formation through gasification, leading to a homogeneous initial pore structure with a very narrow pore size distribution.[30] Additionally, the evaporation of compounds derived from the chemical activating agent in previously occupied spaces contributes to the formation of cavities on the activated carbon surface. These cavities act as primary channels, connecting to the inner surface of AC through micropores.[47]

As shown in Table 4, the specific surface area, micropore volume, and micropore distribution relative to the total pore volume of POMCO$_2$-AC are 1100 m^2 g^{-1}, 0.45 cm^3 g^{-1}, and 83%/0.54, respectively—values that are several times higher than those of the solely carbonized peanut shell (BC). These results indicate that AC activated using a physical–chemical activation technique significantly enhances the physical properties of peanut shells. Such improvements facilitate better access to active sites and enhance the diffusion of small molecules such as DCM during adsorption. Furthermore, SEM analysis confirms the well-developed porous structure of the produced AC.

The FT-IR spectra of activated carbon (POMCO$_2$-AC) derived from peanut shells was obtained to identify the functional groups present on the carbon surface. The spectrum displays various bands, as shown in Fig. 6. A peak around 3425 cm^{-1} is associated with the stretching vibrations of hydroxyl (O–H) functional groups.[67] Bands appearing at approximately 2921 cm^{-1} and 2854 cm^{-1} correspond to aliphatic C–H stretching vibrations.[68] The peak at 1977 cm^{-1} is possibly linked to C=C=C stretching, allene.[69] The band at 1623 cm^{-1} is attributed to aromatic rings or C=C stretching vibrations[35] and may also indicate the presence of highly conjugated carbonyl groups.[37] The presence of C–O stretching vibrations around 1124 cm^{-1} is likely associated with alcoholic, phenolic, and carboxylic groups in POMCO$_2$-AC.[37,68]

The chemical properties of activated carbons are primarily shaped by variations in surface chemistry, influenced by heteroatoms such as oxygen, nitrogen, hydrogen, sulfur, and phosphorus within the carbon structure. These elements may originate from the raw material or be introduced during activation. The surface functional groups formed by these heteroatoms, along with the delocalized electrons in the carbon matrix, determine whether the activated carbon surface exhibits acidic or basic characteristics.[70]

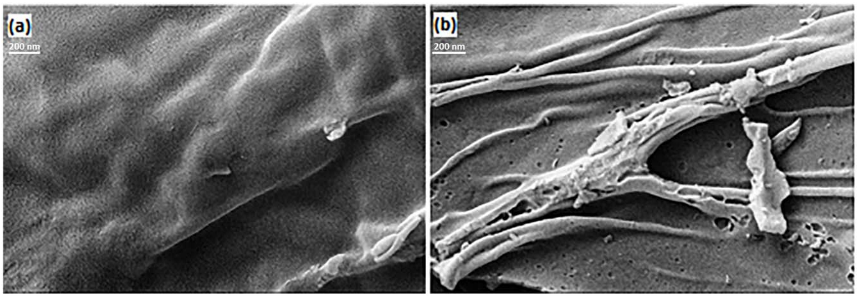

Fig. 5 FESEM images of (a) peanut shell, (b) POMCO$_2$-AC.

Table 4 Adsorption data for DCM on adsorbents reported in other literature and this work

No.	Type of adsorbent	S_{BET} (m^2 g^{-1})	Initial concentration	Adsorption method	T (°C)	q_e (mg g^{-1})	Ref.
1	POMCO$_2$-AC	1100	2000 ppmv	Dynamic	25	217	This work
2	Commercial AC-1	986	2000 ppmv	Dynamic	25	159	This work
3	FAU zeolite (NaY)	657	Pure DCM	Static	30	212[a]	76
4	Commercial AC-2	1000	Pure DCM	Static	30	378[a]	77
5	Commercial AC-3	973	≈3000 ppmv	Dynamic	23	120	78
6	ZG-15	559	≈140 ppmv	Dynamic	Room	240	79

[a] @ Relative pressure ≈ 1.

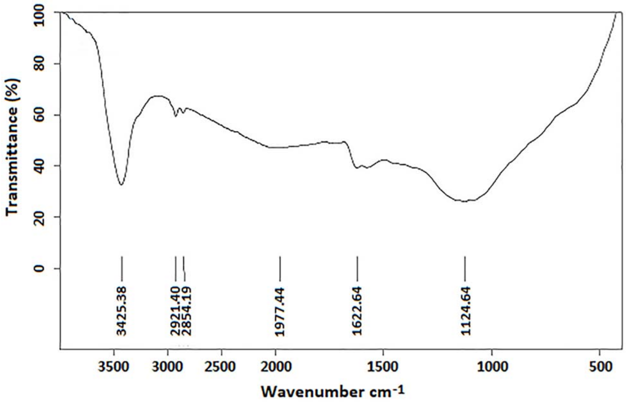

Fig. 6 FT-IR spectra for the POMCO$_2$-AC.

The acidic properties of activated carbons largely stem from oxygen-containing groups, including carboxylic acids, anhydrides, lactones, and phenols. In contrast, surface basicity is associated with the resonating π-electrons in aromatic carbon rings that attract protons, nitrogen-based functionalities capable of proton binding, as well as oxygen-free Lewis sites and structures like carbonyl, pyrone, and chromene located at the carbon layer edges.[51,71]

Meanwhile, the parameter pHpzc (pH at the point of zero charge) offers valuable insights into the acidity, basicity, and surface charge of activated carbon, aiding in a deeper understanding of its adsorption mechanism.[72]

There is no standard method for determining pH_{pzc} and in this study we used the method of Foo and Hameed.[73] The pH_{pzc} value for peanut shell was found to be 6.23, which aligns with the value obtained by Banerjee and colleagues.[74] Additionally, the pH_{pzc} value for the activated carbon POMCO$_2$-AC was determined to be 6.75, which was almost consistent with the value obtained by Foo *et al.*[38] The increase in pH_{pzc} after PS carbonization and activation is due to an increase in the number of aromatic groups containing oxygen or oxygen-free Lewis sites on the POMCO$_2$-AC surface.[71] The prepared peanut shell activated carbons are negatively charged above pH 6.75. The surface basicity of AC could enhance the electrostatic interaction between porous carbon and acid molecules, such as dipole–dipole, van der Waals, and so on. This feature can also positively affect the physical adsorption and thus the adsorption capacity of the produced AC. In this regard, Cazetta *et al.* showed that the MB adsorption is favored due to the acid characteristics of the AC surface, which was described by pH_{pzc}.[72] Most of the oxygen groups are the source of surface acidity, which contributes to the adhesive of hydrophilic Volatile organic compounds (VOCs) onto carbon surface.[75]

Overall, the results from FTIR analysis (comparing the intensities of the wavelengths at 3425 cm^{-1} and 1623 cm^{-1}), CHNSO analysis (the low oxygen content in POMCO$_2$-AC activated carbon), and the pH_{pzc} value of POMCO$_2$-AC indicate that the surface of the synthesized activated carbon in this study exhibits a less acidic nature. On the other hand, it is evident that dichloromethane (CH_2Cl_2) is a polar hydrocarbon. Chlorine is more electronegative than hydrogen, thus exerting a greater "pull" on the electrons. The net dipole moment in the mentioned case does not cancel out, unlike in carbon tetrachloride. As a result, when DCM is in contact with the POMCO$_2$-AC adsorbent, an electrical attraction occurs at the surface of the activated carbon with the adsorbate. This implies that adsorption depends not only on the physical characteristics of the adsorbent structure but also on the chemical structure of the adsorbent surface.

Given the moderate polarity of dichloromethane compared to alcohols, amines, or organic acids, a moderately polar surface of activated carbon can result in better interactions. Consequently, reducing the surface acidity of the activated carbon—meaning a decrease in polar functional groups, such as hydroxyl or carboxyl—has led to improved adsorption of dichloromethane.

It is important to note that chemisorption does not occur here, as chemisorption involves the formation of a covalent bond between the adsorbate and the adsorbent substrate through the sharing or transfer of electrons. Therefore, physical adsorption occurs due to electrostatic interactions, including dipole–dipole forces and van der Waals interactions, where bonds can be easily broken due to weak interactions.

The most key factor play important roles in VOC adsorption onto carbon materials is physical–chemical characteristics of the adsorbents (such as: specific surface area, pore structure and surface chemical functional groups, *etc.*). Other influencing factors on the adsorption capacity of VOCs with engineered carbon materials are as following: (1) properties of adsorbate molecule (such as: the molecular structure, polarity, *etc.*), and (2) adsorption conditions (such as: temperature, pressure, humidity, gas flow rate, *etc.*).

Based on the studies conducted up to now, dichloromethane has been removed using various types of adsorbents mentioned in Table 4.

As seen in Table 4, the adsorption capacity of DCM on the synthesized activated carbon (POMCO$_2$-AC) in this work is higher than adsorption capacities of other adsorbents, except for the commercial AC-2 and the composite adsorbent ZG-15. For example with regard to the Borkar *et al.* report, the adsorption capacity near to the saturation pressure of DCM on commercial AC-2 was found to be about 4.5 (mol kg^{-1}) or 378 (mg g^{-1}).[77] In addition, according to the Zhou and his colleagues, the high DCM adsorption capacity of the adsorbent ZG-15, which is a composite of ZIF-8 with graphene oxide (GO), was due to the synergistic effects of the interactions between ZIF-8 and GO, or more precisely, the surface chemistry and strong interactions between some of the groups of GO molecules and methylene chloride.[79] Based on the characterization analysis results of the POMCO$_2$-AC, the high DCM adsorption capacity can be associated with the well developed porous structure and surface chemistry of the prepared AC in this study.

3.2 Model development, statistical analysis, evaluation, and results

Based on the CCD experimental design used in this study, the total number of tests was 20, including 15 tests with five repetitions at the central point to identify errors. Independent variables with coded and real values, along with the observed and predicted test results, are summarized in Table 5.

The statistical significance of the regression terms was examined using ANOVA (analysis of variance). The ANOVA results for the AC production yield (Y_{AC}) in (%) and the specific surface area (S_{BET}) of activated carbon in (m^2 g^{-1}), along with the corresponding multiple determination coefficients (R^2) are presented in Table 6.

Using the quadratic models (eqn (5) and (6)) and performing multiple regression analysis, the responses for Y_{AC} (%) and S_{BET} (m^2 g^{-1}) along with the test variables were calculated as follows:

$$\begin{aligned} Y_1 = {} & 1063.31 + 40.01X_1 + 52.22X_2 + 77.73X_3 \\ & - 27.87X_1X_2 - 6.29X_1X_3 + 9.18X_2X_3 \\ & - 57.53{X_1}^2 - 67.37{X_2}^2 - 79.13{X_3}^2 \end{aligned} \tag{5}$$

$$\begin{aligned} Y_2 = {} & 19.41 + 0.1803X_1 - 2.77X_2 - 5.07X_3 \\ & - 0.3950X_1X_2 - 0.0675X_1X_3 - 0.9100X_2X_3 \\ & - 0.4430{X_1}^2 + 0.6601{X_2}^2 + 0.3437{X_3}^2 \end{aligned} \tag{6}$$

To evaluate and validate the fit of the empirical models, it is necessary to assess both their accuracy and precision. Model accuracy can be evaluated using charts generated by the software, based on actual data (test results), predicted responses, and residuals. The precision of the model can be tracked through the table of ANOVA results, the *p*-value, and determination coefficient (R^2).[59–61,67]

In evaluating model precision, the *p*-value must be less than 0.05 at a 95% confidence level. Additionally, the *p*-value for Lack of Fit should be greater than 0.05. In other words, the model should be significant, and the Lack of Fit should not be significant. According to the results in Table 5, the precision of

Table 5 CCD design with observed and predicted values

		Independent variable						Response			
								Y_1 (S_{BET})		Y_2 (Y_{AC})	
		Real value			Coded value						
Standard order	Categorical factor level	X_1	X_2	X_3	X_1	X_2	X_3	Observed value (m^2 g^{-1})	Predicted value (m^2 g^{-1})	Observed value (%)	Predicted value (%)
1	Factorial points (8 points)	0.4	700	1.8	−1	−1	−1	655.5	664.3	26.3	26.3
2		1.5	700	1.8	+1	−1	−1	817.0	812.7	27.6	27.6
3		0.4	800	1.8	−1	+1	−1	800.1	806.2	23.3	23.3
4		1.5	800	1.8	+1	+1	−1	852.2	843.0	23.1	23.0
5		0.4	700	7	−1	−1	+1	803.2	814.0	18.2	18.1
6		1.5	700	7	+1	−1	+1	941.6	937.2	19.2	19.1
7		0.4	800	7	−1	+1	+1	986.6	992.6	11.6	11.5
8		1.5	800	7	+1	+1	+1	1011.5	1004.2	11.0	10.9
9	Star points (6points)	0	750	4.4	−1.68	0	0	851.4	833.3	17.8	17.9
10		1.9	750	4.4	+1.68	0	0	925.2	967.9	18.8	18.5
11		0.9	666	4.4	0	−1.68	0	790.7	784.9	25.8	25.9
12		0.9	834	4.4	0	+1.68	0	957.2	960.6	16.5	16.6
13		0.9	750	0	0	0	−1.68	708.8	708.8	28.9	28.9
14		0.9	750	8.8	0	0	+1.68	972.5	970.2	11.7	11.9
15	Central points (6 points)	0.9	750	4.4	0	0	0	1022.9	1063.3	19.7	19.4
16		0.9	750	4.4	0	0	0	1082.2	1063.3	19.2	19.4
17		0.9	750	4.4	0	0	0	1066.3	1063.3	19.4	19.4
18		0.9	750	4.4	0	0	0	1072.2	1063.3	19.3	19.4
19		0.9	750	4.4	0	0	0	1070.5	1063.3	19.2	19.4
20		0.9	750	4.4	0	0	0	1065.4	1063.3	19.6	19.4

Table 6 Analysis of variance (ANOVA) for response surface quadratic models on the S_{BET} (Y_1) and yield (Y_2) of activated carbon

	Sum of squares		df		Mean square		*F*-value		*p*-Value		Result	
Source	Y_1	Y_2	Y_1	Y_2	Y_1	Y_2	Y_1	Y_2	Y_1	Y_2	Y_1	Y_2
Model	3.19×10^5	476.03	9	9	35 488.65	52.89	110.91	1582.70	<0.0001	<0.0001	Significant	
X_1-IR	21 860.03	0.44	1	1	21 860.03	0.44	68.32	13.29	<0.0001	0.0045		
X_2-T_{act}	37 235.88	105.07	1	1	37 235.88	105.07	116.37	3144.08	<0.0001	<0.0001		
X_3-CO_2 rate	82 511.62	351.02	1	1	82 511.62	351.02	257.86	10 503.59	<0.0001	<0.0001		
X_1X_2	6215.57	1.25	1	1	6215.57	1.25	19.42	37.35	0.0013	0.0001		
X_1X_3	316.89	0.037	1	1	316.89	0.037	0.9903	1.09	0.3431	0.3209		
X_2X_3	674.00	6.62	1	1	674.00	6.62	2.11	198.24	0.1773	<0.0001		
X_1^2	47 694.66	2.83	1	1	47 694.66	2.83	149.05	84.61	<0.0001	<0.0001		
X_2^2	65 411.63	6.28	1	1	65 411.63	6.28	204.42	187.92	<0.0001	<0.0001		
X_3^2	90 238.63	1.70	1	1	90 238.63	1.70	282.01	50.94	<0.0001	<0.0001		
Residual	3199.87	0.33	10	10	319.99	0.03						
Lack of fit	1066.13	0.10	5	5	213.23	0.02	0.4997	0.45	0.7677	0.7980	Not significant	
Pure error	2133.74	0.23	5	5	426.75	0.05						
R^2											0.99	0.999
Adjusted R^2											0.98	0.999
Predicted R^2											0.97	0.998
Adeq precision											31.54	139.04

the models is confirmed. Furthermore, the high determination coefficient ($R^2 > 0.99$) for both models indicates strong agreement between actual and predicted values.

To evaluate model adequacy, residual normal plot, predicted *vs.* actual, and residual *vs.* predicted plots are used. Fig. 7 displays these plots.

Fig. 7(a_1) and (b_1) show the normal probability plots of the residuals. As can be seen in the figures, due to the randomly points distribution around the bisector line, residuals conform a normal distribution. Predicted *vs.* actual plots (Fig. 7a_2 and 7b_2) are scatter plots that help visualize the performance of a regression model. Ideally, if the predictions are perfect, the points will lie along a straight line with a slope of 1. As can be observed, the suggested responses describe the experimental values well. Plot of residuals *versus* predicted responses values are displayed in Fig. 7(a_3) and (b_3). AS can be observed, the points are distributed randomly between two red lines. If responses deviate from these lines, it suggests a need for transformation. The figures show that transformations are not necessary for the responses. These assessments help validate the accuracy of the model based on how well predicted values align with actual experimental data across different evaluation plots.

Therefore, the accuracy and validity of the developed models for both responses are confirmed, and the models are considered reliable.

Fig. 8–10 show the 3-D and counter plots of responses based on variables.

3.2.1 The combined effects of T_{act} and IR on the S_{BET} and Y_{AC}. Fig. 8 shows that (1) the maximum value of S_{BET} and Y_{AC} occured around the midpoint of IR and T_{act}. (2) With the simultaneous increase of both variables, the S_{BET} and AC production yield decrease. The following chemical reactions are predicted to occur between the potassium oxalate (PO) and the carboneous precursor:[19,49]

$$\text{(PO)}K_2C_2O_4 \rightarrow \text{(PC)}K_2CO_3 + CO \tag{7}$$

$$\text{(PC)}K_2CO_3 + 2C \rightarrow 2K + 3CO \tag{8}$$

$$K_2CO_3 \rightarrow K_2O + CO_2 \tag{9}$$

$$K_2O + 2C \rightarrow 2K + CO \tag{10}$$

An increase in potassium oxalate concentration, based on probable reactions during activation, leads to a higher presence of its derivatives in the process. This can cause mesopore destruction and pores blockage due to tar accumulation, ultimately reducing accessible surface area, lowering production yield, and increasing carbon precursor burn-off.[40,50,51]

On the other hand, while increasing the temperature promotes the formation of microporous structure, a simultaneous rise in both temperature and impregnation ratio accelerates the cracking of organic material.[36,52]

3.2.2 The combined effects of T_{act} and gas flow rate of CO_2 on the S_{BET} and Y_{AC}. As shown in Fig. 9, the interaction between activation temperature and the concentration of the physical activation agent (CO_2) positively influences the surface area (S_{BET}) of the carbon adsorbent, while exerting an inverse effect on production yield. In other words, a simultaneous increase in temperature and CO_2 gas flow rate slightly enhances the S_{BET} surface area during gasification but reduces yield due to the higher percentage of burn-off.[80] The optimal point lies within the mid-range of these two variables.

3.2.3 The combined effects of IR and gas flow rate of CO_2 on the S_{BET} and Y_{AC}. Fig. 10 illustrates that when both the CO_2 flow rate and IR increases up to their midpoint, the S_{BET} also rises, as these factors individually have a positive effect on the response. However, increasing the variables beyond a certain value from the midpoint range causes a decrease in the S_{BET} of the activated carbon. The thermal decomposition of potassium oxalate (based on reactions 1 to 4) and the formation of

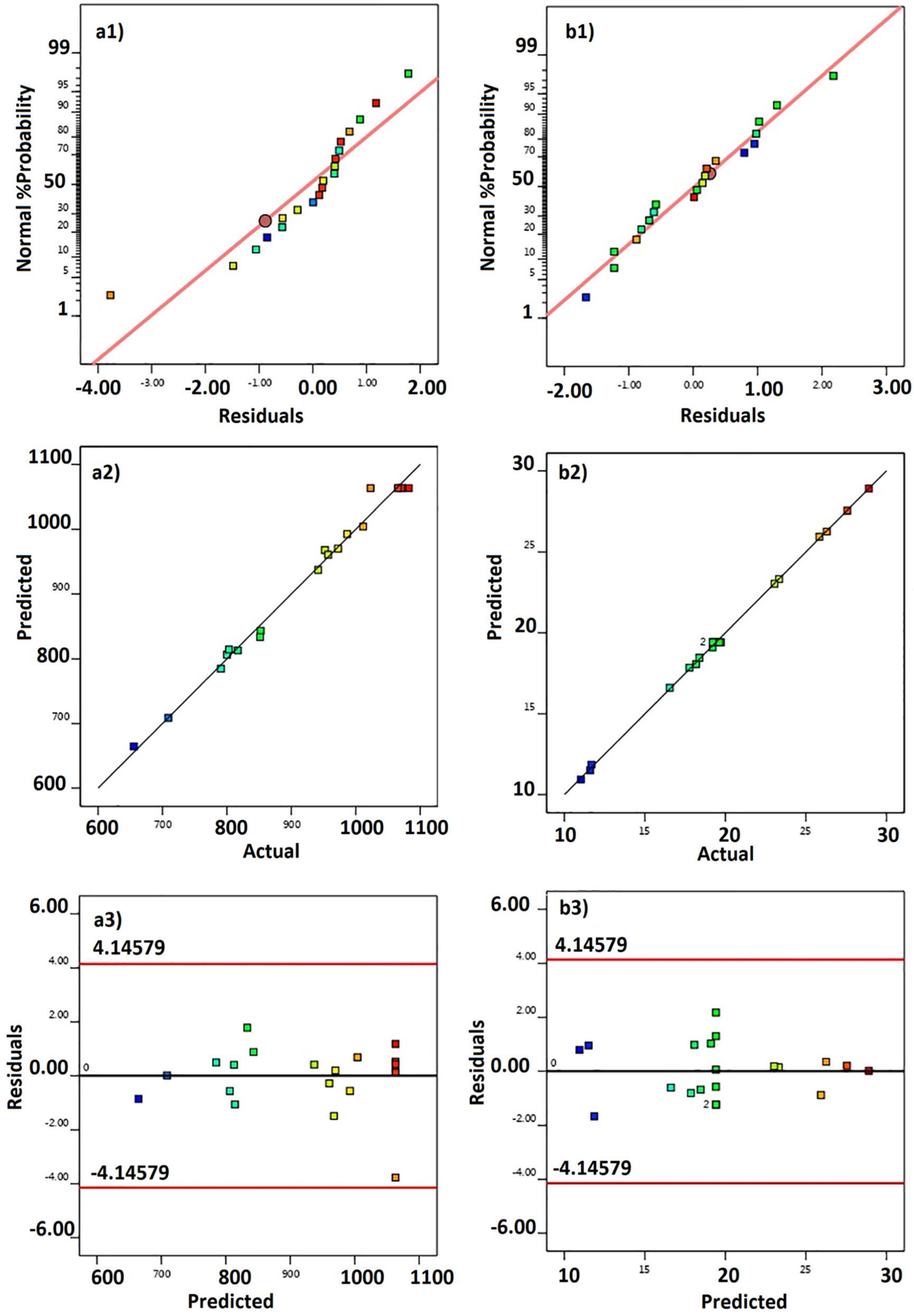

Fig. 7 Assessment of the CCD predictive correlation for (a) S_{BET} and (b) Yield (%). 1, 2, and 3 indicate Residual normal probability plot, predicted *versus* actual values plot, and residual *versus* predicted response plot, respectively.

additional moles of CO at approximately 570 °C, along with the gasification of carbon with CO_2 at temperatures above 700 °C due to the reaction $C + CO_2 \rightarrow 2CO$, contribute to both the pore formation and the drilling of pores. This process facilitates pore opening and acts as a carrier gas to remove volatile substances from the charcoal matrix, thereby increasing the degree of

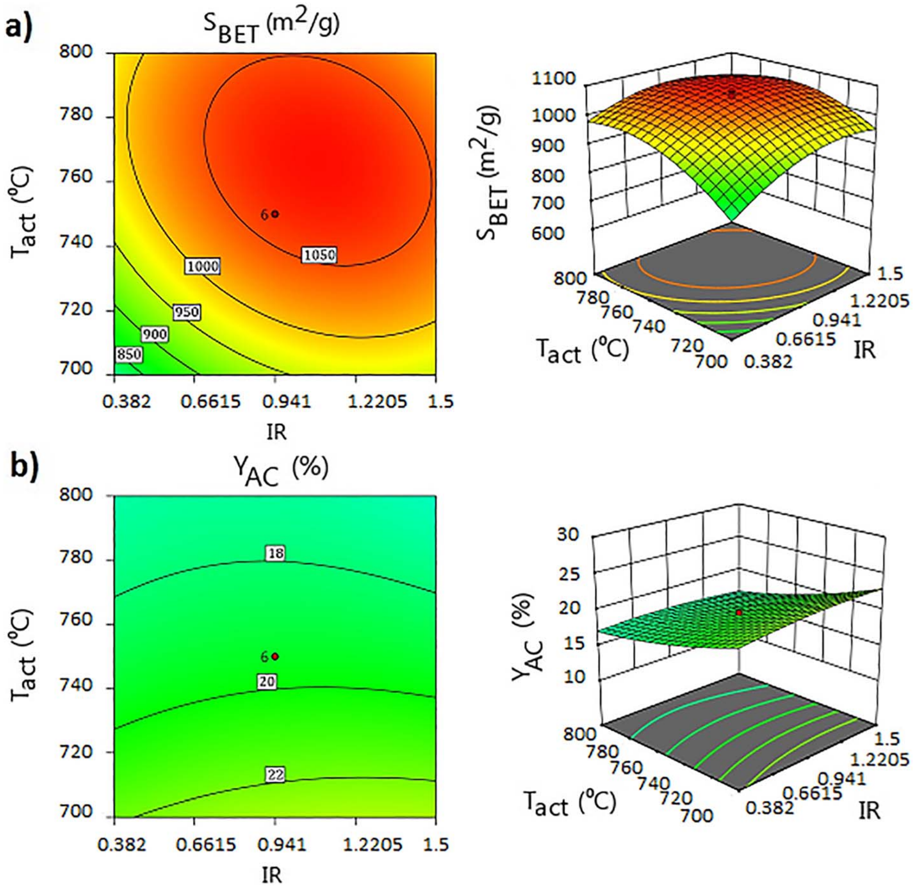

Fig. 8 3D response surfaces and contour plots for effects IR & T_{act} on (a) S_{BET}, (b) Y_{AC} at central point of CO_2 gas flow rate = 4.4 L h^{-1}.

activation. The combined use of physical and chemical activation provides a beneficial buffering effect to some extent. However, excessive increases in either potassium oxalate concentration or CO_2 gas flow rate can lead to CO overproduction during activation, creating highly aggressive conditions. This results in excessive pore widening (conversion of micropores to macropores), which negatively impacts surface area expansion and subsequently reduces the S_{BET}. As expected, this is also accompanied by a decrease in production yield.[49,67] To determine the optimal conditions for maximizing S_{BET} and Y_{AC} in PS – activated carbon within the studied experimental ranges, the desirable point prediction function in the design-expert software was applied. The predicted optimal results for POMCO$_2$-AC were obtained using a T_{act} of 746 °C, an IR of 1.14 and a CO_2 gas flow rate of 4.14 L h^{-1}. The predicted S_{BET} and Y_{AC} values for POMCO$_2$-AC were 1059 m^2 g^{-1} and 20.14%, respectively. To validate these predictions, several POMCO$_2$-AC samples were prepared under the identified optimum conditions. The average experimental values obtained for S_{BET} and Y_{AC} were 1100 m^2 g^{-1} and 20.58%, respectively, demonstrating strong agreement with the predicted values from the regression models, with relatively small errors of 3.9% and 2.2%, respectively.

3.3 Adsorption isotherm modeling

The adsorption capacity of a pollutant can be assessed through adsorption isotherms, which illustrate the equilibrium relationship between the adsorbent and adsorbate.[81] The isotherm shape reveals insights into the stability of interactions between these components and indicates the adsorption affinity of the molecules involved. Additionally, parameters derived from various models offer valuable information regarding the mechanisms of sorption, as well as the surface properties and affinities of the adsorbents.

Up to now, various mathematical models have been developed and used to describe experimental data of adsorption isotherms. In this study, the experimental adsorption equilibrium data at different temperatures were analyzed by Langmuir, Freundlich and Langmuir–Freundlich adsorption isotherms.

The Langmuir and Freundlich models are the most accepted surface adsorption model for single adsorbate systems.[82] The Langmuir and Freundlich isotherms are known as two-parameter models, which provide information on the adsorption capacity and constants related to the activation energy. The Langmuir–Freundlich isotherm is known as three-parameter model, which is a combination of Freundlich and Langmuir isotherm models.

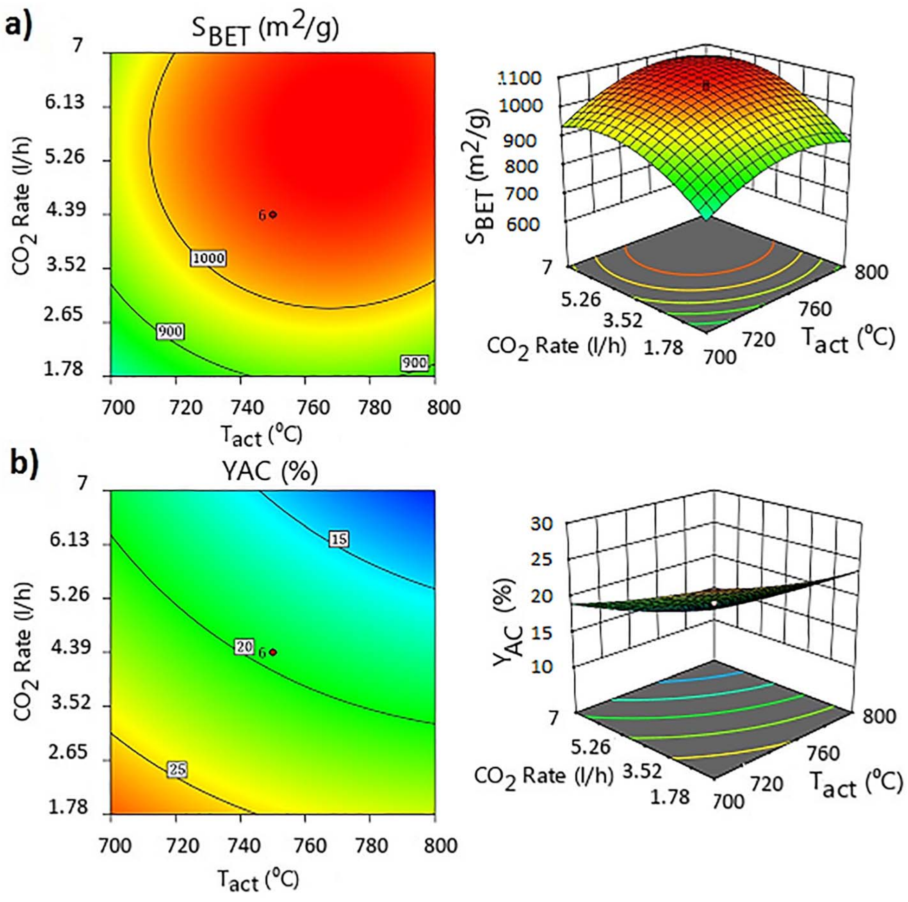

Fig. 9 3D response surfaces and contour plots for effects CO_2 gas flow rate & T_{act} on (a) S_{BET}, (b) Y_{AC} at central point of IR = 0.941 g g^{-1}.

Nonlinear regression approach was employed to fit adsorption isotherm models to the experimental data, utilizing MATLAB software (fmincon, constrained non linear multivariable function). The advantage of nonlinear regression is that it minimizes errors resulting from linearization.[54]

In this work, adsorption isotherm experiments were conducted with varying initial concentrations of 0–3000 ppmv under the temperature range of 273–323 K.

According to Fig. 11, the isotherm curves show the overlay of the experimental results (points) and the calculated theoretical points (lines).

The first step and one of the most important conditions for selecting any isotherm model is that there should be a good fit between the experimental data and the isotherm function. Typically, isotherm models are evaluated against statistical data such as R^2, χ^2, SSE, and also Marquardt's percent standard deviation (MPSD). The determination coefficient (R^2) reflects the quality of fit between experimental data and the nonlinear adsorption equations. For instance, if the R^2 is close to one, it indicates the model provides the best fit. Whereas nonlinear chi-square (χ^2) shows the fit between experimental values and predicted adsorption capacity, used for plotting adsorption isotherm curves. A higher reduced chi-square value ($\chi^2 > 1$) suggests a poor fit. Moreover, sum square error (SSE) indicates how much the calculated values using the adsorption isotherm model can differ from the experimental data. If the error value is small, it means that the isotherm data closely matches the experimental data. The expressions for R^2, χ^2, SSE, and MPSD were calculated using the following relationships:[83]

$$R^2 = \frac{\sum_{i=1}^{m} (y_c - \bar{y}_e)_i^2}{\sum_{i=1}^{m} (y_c - \bar{y}_e)_i^2 + \sum_{i=1}^{m} (y_c - \bar{y}_e)_i^2} \tag{11}$$

$$\chi^2 = \sum_{i=1}^{m} \left[\frac{(y_e - y_c)^2}{y_c} \right]_i \tag{12}$$

$$\text{SSE} = \sum_{i=1}^{m} (y_c - y_e)_i^2 \tag{13}$$

$$\text{MPSD} = 100\sqrt{\frac{\sum \left[(q_{\text{exp}} - q_{\text{mod}})/q_{\text{exp}} \right]^2}{N - p}} \tag{14}$$

The modeling results and the statistical data at different temperatures are summarized in Table 7.

The next step to ensure the thermodynamic feasibility of the selected model, it is essential that the isotherm model meets three specific conditions:

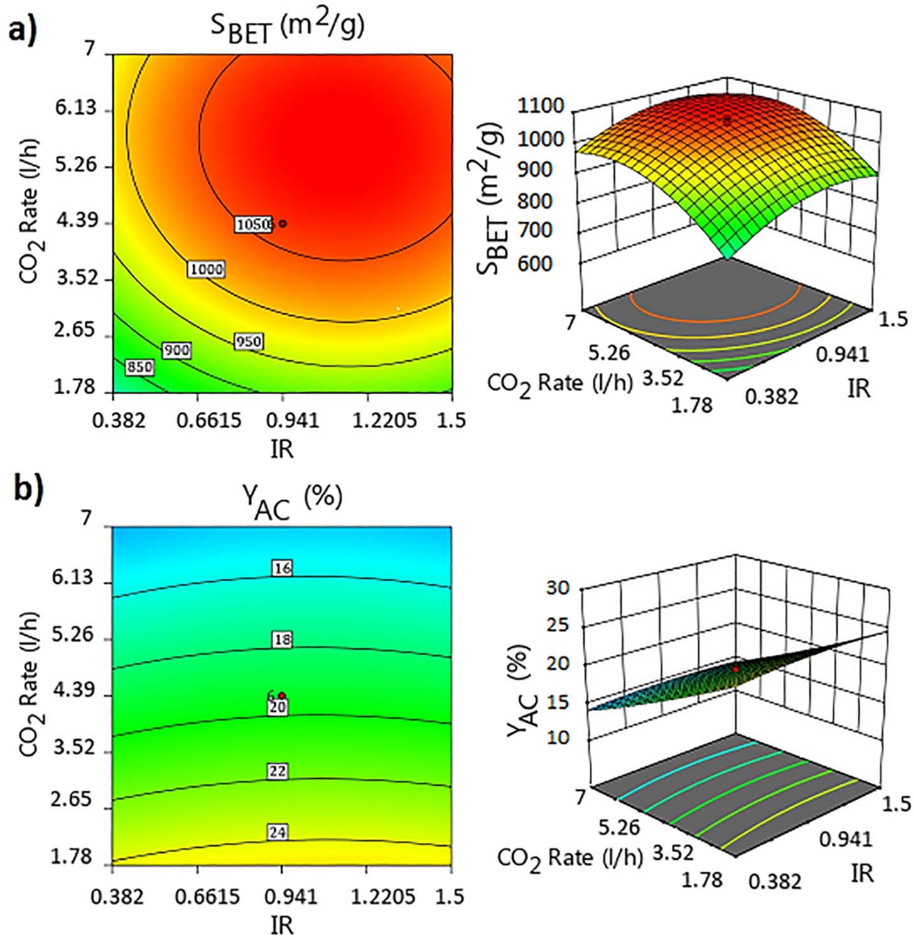

Fig. 10 3D response surfaces and contour plots for effects CO_2 flow rate & IR on (a) S_{BET}, (b) Y_{AC} at central point of $T_{act} = 750$ °C.

1. The isotherm should exhibit linearity at zero concentration.

2. A finite capacity should be present at maximum concentration.

3. The gradient of the function must remain positive across all concentration levels.

Henry's law fulfills the first condition, while the second condition reflects the adsorption limitations posed by surface area and pore volume. However, certain isotherm models, such as the Freundlich model, do not impose an upper boundary for capacity at high concentrations. The third condition is particularly important, as it prevents a physically unrealistic decrease in capacity with increasing concentration, an issue that can sometimes arise in polynomial isotherm models.[33,54]

The Langmuir isotherm was originally developed to describe the gas–solid phase adsorption of activated carbon based on fundamental assumptions. Later, its application was extended to empirically describe equilibrium relationships between a bulk liquid phase and a solid phase.[33,72] According to the results presented in Table 7, the q_m values obtained from Langmuir isotherms were 297.8, 235.7, and 165.8 mg g^{-1} and the R^2 values were 0.996, 0.996, and 0.992 at 273, 298, and 323 K, respectively. The q_m is close to the experimental values, which are 275.3, 217, and 147.3 mg g^{-1}. Also, the nature of adsorption on basis of Langmuir model can be expressed in terms of dimensionless equilibrium parameter (R_L). The values of R_L indicate the type of isotherm to be irreversible ($R_L = 0$), favorable ($0 < R_L < 1$), linear ($R_L = 1$) or unfavorable ($R_L > 1$). In present work, R_L value is $0 < R_L < 1$ which indicates that the DMC-(POMCO$_2$-AC) system is favorable.

The Freundlich model is an empirical equation based on the adsorption on heterogeneous surface and multilayer adsorption.[72] The heterogeneity factor (n) indicates whether the adsorption process is linear ($n = 1$), chemical ($n < 1$) and or physical ($n > 1$). Additionally, the value of $1/n < 1$ indicates a normal Langmuir isotherm while $1/n > 1$ is an indicative of cooperative adsorption. The values of n (4.212, 4.106, 3.583) and $1/n$ (0.24, 0.24, 0.28) at 273, 298, and 323 K, respectively, indicate that the adsorption is physical and the POMCO$_2$-AC is good adsorbent for DCM. As shown in Table 7, the R^2 values for the Freundlich isotherm model across different temperatures were lower compared to other models, ranging between 0.96 and 0.98. The Langmuir–Freundlich model is a combination of the characteristics of the Langmuir and Freundlich isotherms.[55] This isotherm is the application of Langmuir isotherm on a heterogeneous surface.[84] The parameter K_{LF} defines the intensity of adsorbent and adsorbate interactions, and mLF represents the heterogeneity and favorability. The Langmuir–

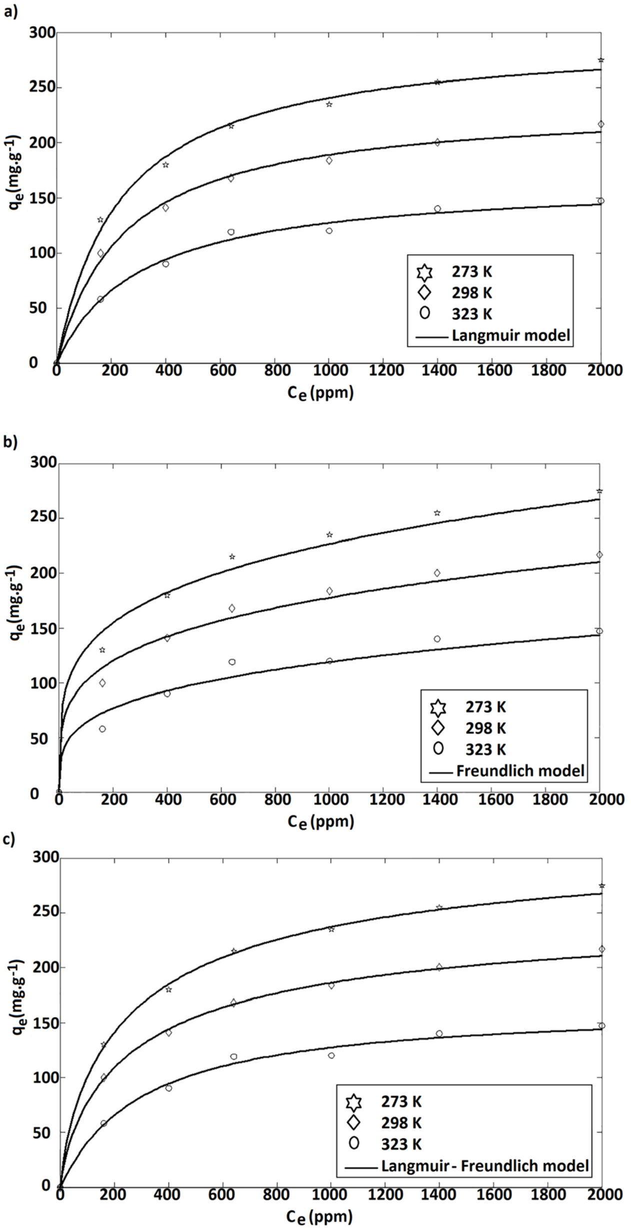

Fig. 11 A comparison of the experimental and predicted adsorption isotherms of DCM on POMCO$_2$-AC surface at different temperatures using (a) Langmuir, (b) Freundlich, and (c) Langmuir–Freundlich equations.

Freundlich equation (Table 7) reduces to Langmuir for mLF = 1. In the present study, mLF is close to the unit value, which reduces the Langmuir equation. Additionally, the model provided values of q_m and R^2 equals to 326.3, 257, 164.7 mg g^{-1} and 0.998, 0.998, 0.992 at 273, 298, and 323 K, respectively. As shown in Fig. 11, the plots of the Langmuir and Langmuir–Freundlich isotherm models demonstrate a strong fit with the experimental data, whereas the plots of the Freundlich isotherm model exhibit a weaker fit. Across all temperature conditions, the Langmuir and Langmuir–Freundlich models exhibited high correlation coefficient values (>0.99), signifying a strong alignment with the experimental data. A close similarity was also observed between these two isotherm models. The error functions SSE and χ^2 were favorable and nearly identical for both models.

As shown in Table 7, the MPSD value for the Langmuir model was less than 8%, underscoring its superiority over the other models. Consequently, among the three isotherm models examined in this study, the Langmuir isotherm model provided the most precision representation of DCM adsorption onto POMCO$_2$-AC. Moreover, small variations in MPSD across different temperature ranges indicate greater stability and predictability in the Langmuir and Langmuir–Freundlich models compared to the Freundlich model.

Furthermore, all three models are thermodynamically acceptable, as they satisfy the three conditions mentioned above.

Scientific progress is restricted when experimental measurements lack reproducibility. Given this, we analyzed the adsorption test results separately for both operating modes. In the dynamic adsorption mode, adsorption capacity of activated carbon was measured under identical experimental conditions across four repetitions. The initial statistical calculations showed that no data outliers were present in the measurements. Additionally, the maximum difference in the obtained results is ±2%, confirming the complete reprodiucibility of dynamic adsorption tests. Subsequently, the reprodiucibility of responses in the static adsorption mode was examined. This concept was assessed through adsorption isotherms. Due to the complexity and time-consuming nature of these experiments, equilibrium adsorption tests were conducted only at 298 K across two orders. The Langmuir isotherm model is the sole functional form applied in this study. In this scenario, due to $N = 2$ reliable identification of outliers is not feasible, defining an outlier level of 3. Statistical results indicate that in both orders, the root-meansquare error (RMSE) remains <MPSD/2, suggesting that the isotherms exhibit moderate consistency rating and a reprodiucibility level of R3.[85]

3.4 Adsorption kinetics

Kinetic studies are essential for the design and modeling of the adsorption process, as well as for a better understanding of adsorption dynamics. In this study, various kinetic models, such as pseudo-first-order, pseudo-second-order, and intraparticle diffusion (eqn (20)–(22)), were employed. To identify the most suitable kinetic model for describing the experimental data, the correlation coefficient (R^2) and normalized standard deviation (eqn (21)) were utilized. Adsorption kinetic experiments were conducted with an initial dichloromethane (DCM) concentration of 2000 ppmv at 298 K.

Adsorption kinetic models were fitted to the experimental data using nonlinear regression analysis, performed with MATLAB software. Fig. 12(a) and (b) illustrate the non-linear plots corresponding to the pseudo-first order and pseudo-second order kinetic models, respectively.

Table 8 presents a comparison of all kinetic parameters, the correlation coefficient (R^2), and Δq (%) values obtained at various temperatures.

Table 7 Parameter estimates and statistical metrics for models fit of the DCM isotherm data[33,55,56]

				Temperature (K)		
Isotherm model	Eqn	Non-linear form	Parameters	273	298	323
Langmuir	(15)	$q_e = \frac{q_m b C_e}{1 + bC_e}$	q_m	297.8	235.7	165.8
			b	0.0042	0.0040	0.0033
			R_L[a]	$0.07 < R_L < 0.59$	$0.08 < R_L < 0.61$	$0.09 < R_L < 0.65$
			R^2	0.996	0.996	0.992
			SSE	269.1	155.2	149.1
			χ^2	1.5	1.1	1.3
			MPSD	7.5	7.4	7.6
Freundlich	(16)	$q_e = K_F C_e^{1/n}$	K_F	44	33.0	18.2
			n	4.2	4.1	3.7
			R^2	0.983	0.983	0.964
			SSE	990.6	639.3	675.6
			χ^2	4.9	4.2	7.1
			MPSD	8.9	9.2	13.3
Langmuir–Freundlich	(17)	$q_e = \frac{q_{mLF}(K_{LF}C_e)^{mLF}}{1 + (K_{LF}C_e)^{mLF}}$	q_{mLF}	326.3	257	164.7
			K_{LF}	0.0035	0.0034	0.0033
			mLF	0.78	0.79	1.02
			R^2	0.998	0.998	0.992
			SSE	136.5	81.3	148.8
			χ^2	0.6	0.4	1.2
			MPSD	35.4	35.3	35.7

[a] $R_L = 1/(1 + bC_0)$ (18).

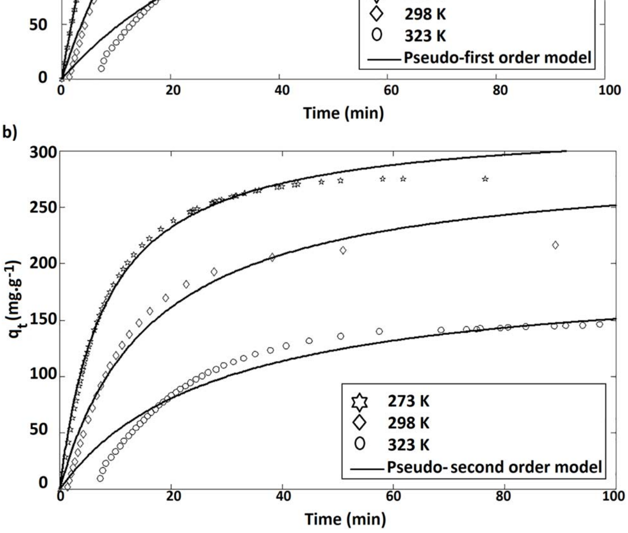

Fig. 12 Adsorption kinetics of DCM in gas phase onto activated carbon at different adsorption temperatures were fitted using (a) pseudo-first order, and (b) by pseudo-second order models.

The normalized standard deviation, Δq (%) defined as:[51]

$$\Delta q = 100\sqrt{\frac{\sum\left[\left(q_{\text{exp}} - q_{\text{mod}}\right)/q_{\text{exp}}\right]^2}{N-1}} \tag{22}$$

where N is the number of adsorption kinetics data points, q_{exp} and q_{mod} (mg g^{-1}) are adsorption capacities of kinetic experiments and models, respectively.

As shown in Fig. 12, the pseudo-first-order kinetic model effectively predicts the adsorption of DCM in the gas phase onto activated carbon, demonstrating satisfactory alignment with the experimental data. Furthermore, the adsorption capacities estimated by the pseudo-first-order kinetic model exhibit better agreement with the experimental results compared to those derived from the second-order model. The pseudo-first-order kinetic model consistently shows the highest R^2 values across all temperatures, whereas the second-order model yields higher Δq values. However, these kinetic models alone are insufficient to fully explain the adsorption mechanism due to the absence of a rate-limiting step.

Generally, the diffusion process of gas into a porous adsorbent comprises three primary regimes: bulk diffusion, boundary layer (film) diffusion, and intraparticle diffusion. To elucidate the adsorption mechanism and identify the rate-limiting step, the adsorption kinetic data were analyzed using intraparticle diffusion model. The results are presented in Fig. 13. The slope of the plot corresponds to the intraparticle diffusion constant (k_{id}), while the intercept value (C) approximates the boundary layer thickness. If the graph of q_t *versus* $t^{1/2}$ forms a straight line passing through the origin, it suggests that intraparticle diffusion is the rate-limiting step.[34]

Table 8 Kinetic model parameters and statistical metrics for adsorption of DCM onto synthesized POMCO$_2$-AC[34,86,87]

Kinetic model	Eqn	Non-linear form	Parameters	Temperature (K) 273	298	323
Pseudo-first order	(19)	$q_t = q_e\left[1 - e^{(-kt1)}\right]$	q_e	268	223	153
			K_1	0.47	0.28	0.15
			R^2	0.998	0.981	0.963
			Δq (%)	0.03	2.06	4.50
Pseudo-second order	(20)	$q_t = \dfrac{k_2 q_e^{\,2} t}{1 + k_2 q_e t}$	K_2	0.0015	0.0008	0.0007
			q_e	327	293	194
			R^2	0.996	0.956	0.934
			Δq (%)	0.08	2.33	4.90
Intraparticle diffusion model	(21)	$q_t = k_{id}t^{0.5} + c$	K_{id}	37	32	15
			C	41	4	9
			R^2	0.88	0.83	0.83

Fig. 13 shows that none of the plots are linear line or pass through the origin, indicating that the intraparticle diffusion model is not the sole rate-limiting step and that adsorption can also be controlled by the boundary layer. Moreover, the R^2 values of the diffusion model are lower than those of the other kinetic models, and the intercept value (C) is relatively large, as detailed in Table 8. These findings suggest that intraparticle diffusion is not the sole rate-limiting step in the adsorption mechanism. Rather, the adsorption of DCM target molecules onto POMCO$_2$-AC is governed by a combination of intraparticle diffusion and other kinetic models, such as boundary layer diffusion.[72]

3.5 Stability test

The stability was conducted by adsorbing to the saturation point on POMCO$_2$-AC activated carbon under operational conditions (at 25 °C, feed gas flow rate of 22 mL min^{-1}, DCM concentration 2000 ppmv, adsorbent bed length of 3 cm), followed by desorption at 200 °C for 2 hours using a nitrogen gas flow. The adsorption–desorption process was repeated five times in this study. After the fifth cycle, the experiments show that the adsorption capacity remained stable, with no significant decrease (less than 2% reduction). Based on these findings, POMCO$_2$-AC activated carbon appears to be a promising candidate for the adsorption of compounds such as DCM in column adsorption operations.[76]

The results of the stability test are presented in Fig. 14.

4. Economic evaluation

For large-scale adsorbent production, both high adsorption performance and economic viability are essential. Balancing activated carbon (AC) quality with cost-effectiveness ensures sustainability and consumer satisfaction. As mentioned in the introduction, the yield of activated carbon (Y_{AC}) is a crucial parameter in evaluating the economic feasibility of the production process. A higher Y_{AC} indicates a more cost-effective production process. Moreover, in economic evaluations, it is essential to account for energy consumption costs—particularly the thermal energy required for carbonization and activation, which directly depend on temperature and process duration—as well as chemical consumption costs, especially the quantity of activating agents needed. Lower consumption of these resources reduces production costs, enhancing economic feasibility. Table 9 shows the performance of ACs on basis of various carbon precursors and activation conditions.

As seen in Table 9, the conclusions are as follows:

1 – The yield of activated carbon (Y_{AC}), calculated based on the weight of raw material, ranges from 6% to 40%, depending on the activation method and operating conditions. This study reports an optimal Y_{AC}.

2 – The specific surface area (S_{BET}) ranges from 80.5 to 2037 m^2 g^{-1}, varying with the activation method and operating conditions. This study presents a desired S_{BET}.

3 – A comparison of conventional activation methods indicates that chemical activation produces activated carbon with

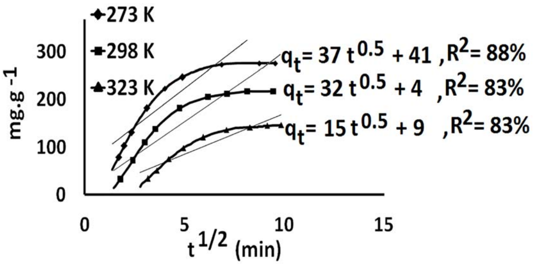

Fig. 13 Intraparticle diffusion plots for the DCM adsorption at different temperatures.

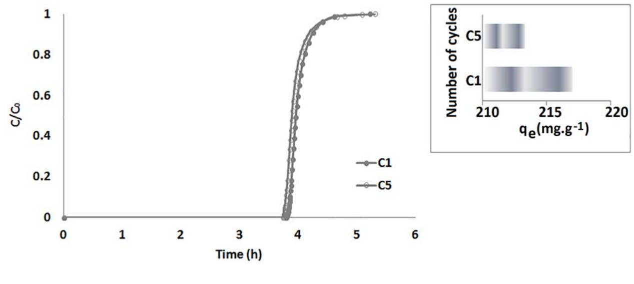

Fig. 14 Breakthrough curve for POMCO$_2$-AC under stability test.

Table 9 Comparison of the performance of activated carbon prepared from different source of precursors and activating agents

			Activation condition				Performance			
No.	Precursor	Activator	CO_2 rate ($L\ h^{-1}$)	IR[a] ($g\ g^{-1}$)	T_{act} (°C)	t_{act} (h)	S_{BET} ($m^2\ g^{-1}$)	Y_{CP}[b] (%)	Y_{AC}[c] (%)	Ref.
1	PS	POM + CO_2	4	1	750	0.5	1100	—	20.6[h]	This work
2[d]	PS[e]	$ZnCl_2$	—	1.8	650	15[f]	1200	40	67	36
3	SOC[e]	K_2CO_3	—	1	600	1	644	—	16.2[h]	40
		KOH	—	1	600	1	600	—	6.3	
4[g]	PC[e]	KOH[e]	—	2	800	1	1310	Unkwon	87.9	41
			—	8	800	1	2037		35.8	
			—	4	900	1	1976		43	
		CO_2	6	—	900	3.5	1980		9.6	
				—	850	3	774		80.5	
5	DP[e]	$FeCl_3$	—	1.5	700	1	780	—	47.1[h]	42
6	PS	KOH[i]	—	1	600[j]	8[f]	1277	—	21.8[h]	43
7[k]	PS	H_3PO_4	—	1	600	1	1091	Unkwon	52	44
		KOH	—				571		54	
8[l]	BMB[e]	CO_2	9	—	900	1	80.5	25.04	19.3[h]	45
9	BFS[e]	$ZnCl_2$	—	1	500	1	560	—	33.7[h]	46
		H_3PO_4	—				905	—	34.4[h]	
		KOH	—				1029	—	30.4[h]	

[a] IR: impregnation ratio or mass ratio of chemical activator/(carbonized or not carbonized) precursor. [b] Carbonized product yield, $Y_{CP}\ (\%) = W_{CP}/W_0 \times 100$, two distinct (carbonization and activation) steps. [c] Activated carbon yield, $Y_{AC}\ (\%) = W_{AC}/W \times 100$, $W = W_0$ or W_{CP}. [d] The first step, PS carbonized at 400 °C for 30 min. [e] PS: peanut shell, SOC: soybean oil cake, PC: polymeric composites, DP: date pit, BMB: barley malt bagasse, BFS: baobab fruit shell. [f] Minutes. [g] The first step, polymer particles carbonized at 850 °C for 2 h. [h] Calculated bases on W_0. [i] Physical mixtures of solid KOH and carbonized particles. [j] Microwave power (W). [k] The first step, PS and deionized (DI) water hydrothermal carbonized at 200 °C for 6 h. [l] The first step, BMB carbonized at 800 °C for 1 h.

a higher surface area and efficiency, while requiring lower temperatures and shorter activation times.

4 – Energy consumption considerations: the temperature and duration of carbonization and activation directly impact the thermal energy required during production, which plays a role in overall economic feasibility. The energy consumption in this work is relatively low. The energy consumption in this study appears to be within a reasonable range.

5 – The chemical activation agent consumption in this work is low (IR = 1).

In this section, a general and quantitative criterion called "adsorbent cost performance" ($\hat{C}$, in \$ mol^{-1}) has been used to offer a straightforward assessment of AC production economic feasibility.[88] The parameter $\hat{C}$ represents the dollar expense required to produce and utilize 1 gram of an adsorbent to eliminate 1 mole of a specified component from the gas phase, calculated based on the maximum adsorption capacity.

To achieve this, the preparation cost of producing 1 kilogram of POMCO$_2$-AC from peanut shells using a single-stage combined physical–chemical activation technique (accounting for an AC yield of 20.6%) has been thoroughly analyzed and reported in Table 10. Subsequently, Table 11 presents the calculated cost of the adsorbent required to remove 1 mole of DCM. The main components required for the production of POMCO$_2$-AC encompass the raw material, transportation, consumables (chemicals and gases), and electrical energy. Notably, this study considers the cost of raw materials and transportation negligible, as peanut shells, an abundant agricultural bio-waste, are readily and freely available in many countries, including Iran.

Table 10 Estimated production cost of POMCO$_2$-AC

	US\$ per kg	
Component	Based on 1 kg produced AC (Y_{AC} = 20.6%)	Ref.
Chemicals (including POM & hydrochloric acid)	1.8	89
Gases (dioxide carbon & nitrogen)	0.9	[a]
Electrical consumption (including carbonization & activation & drying)	1.0	90
Net cost	3.7	
Other overhead costs (10% of net cost)	0.4	
Total	4.1	

[a] On basis of standard refill of CO_2 & N_2 gases in IRAN.

Table 11 Calculation of adsorbent ($POMCO_2$-AC) cost performance

	Target pollutant	Adsorption capacity (mg g^{-1})	Adsorption capacity (g g^{-1})	Molar mass (g mol^{-1})	Adsorption capacity (mol g^{-1})	Total cost of adsorbent (US\$ g^{-1})	$\hat{C}$ (\$ mol^{-1})
Based on produced AC ($Y_{AC} = 20.6\%$)	DCM	217	0.217	84.9	0.003	0.004	1.6

Table 10 indicates that the estimated cost of producing 1 kilogram of $POMCO_2$-AC falls within the global market price range for activated carbon (US\$ 2.2–5 per kg, depending on quality) and is significantly lower than the U.S. activated carbon export price (US\$ 3.68–14,662 per ton).[91,92] This cost efficiency can be attributed to the free availability of raw materials and the activation method used in this research, which requires less chemical and energy consumption during the production process compared to the cases listed in Tables 1 and 2. Considering that the calculated $\hat{C}$ value is lower than 2, as shown in Table 11, $POMCO_2$-AC is categorized as a highly economical adsorbent for the targeted application of removing DCM from the air. Consequently, it can be asserted that the activation technique employed in this study has economically enhanced the value of agricultural waste by converting peanut shell waste into activated carbon ($POMCO_2$-AC), thereby creating a cost-effective alternative to commercial adsorbents available in the market.

5. Conclusion

The optimization of the activated carbon synthesis process using the CCCD experimental design method was successfully conducted. The experimental values obtained for yield and S_{BET} closely matched the values predicted by the second-degree models. The optimal conditions for producing activated carbon ($POMCO_2$-AC) were identified as IR of 1 g g^{-1}, CO_2 rate of 4 L h^{-1}, and T_{act} of 750 °C. The innovative method of integrating chemical activation with POM and physical activation with CO_2 led to the development of greater microporosity compared to mesoporosity, minimal presence of macropores, narrow pore size distribution, and a high specific surface area of 1100 m^2 g^{-1} in the activated carbon. The well-developed porous structure was confirmed by SEM analysis. The CHNSO, FT-IR analysis, and pH_{PZC} tests confirmed that $POMCO_2$-AC has a less acidic nature in its structure. Consequently, the produced activated carbon can exhibit greater affinity for dichloromethane adsorption compared to other similar adsorbents. The results showed that the Langmuir isotherm and pseudo-first-order models described the experimental data better compared to other models. The maximum adsorption capacity (q_{max}) of activated carbon was determined to be 298 mg g^{-1} at 273 K. The adsorption process mechanism was elucidated using the intraparticle diffusion model. However, intraparticle diffusion was not the sole factor influencing the adsorption rate of DCM onto activated carbon; the boundary layer also plays a governing role in the adsorption rate. Stability tests demonstrated that the reused carbon adsorbent could be successfully regenerated and still retain good reusability. Our findings suggest that $POMCO_2$-AC activated carbon, with its optimal physical properties and favorable surface chemistry, serves as an efficient, effective, and economical adsorbent for removing chlorinated volatile organic compounds (Cl–VOCs) such as dichloromethane, making it well-suited for industrial applications.

Abbreviations

b	Langmuir constant related to the free energy of adsorption (L mg^{-1})
C	Intercept (mg g^{-1})
C_e	The equilibrium concentration of the solute in the bulk solution (mg L^{-1})
K_1	Rate constant of pseudo-first order model (min^{-1})
K_2	Rate constant of pseudo-second order model (g mg^{-1} min^{-1})
K_{LF}	The equilibrium constant for a heterogeneous solid
K_{id}	Intraparticle diffusion constant (mg g^{-1} $min^{-1/2}$)
mLF	The heterogeneity parameter, lies between 0 and 1
n	Freundlich constant
N	Number of experimental measurements
p	Number of isotherm parameters
q_t	Adsorption capacity per unit mass of adsorbent at time t (min) (mg g^{-1})
q_m	The maximum adsorption capacity (mg g^{-1})
q_e	Adsorption capacity per unit mass of adsorbent at equilibrium (mg g^{-1})
q_{mLF}	The Langmuir–Freundlich maximum adsorption capacity (mg g^{-1})
q_{exp}	Adsorption capacities of kinetic experiments (mg g^{-1})
q_{mod}	Adsorption capacities of kinetic models (mg g^{-1})
Δq	Normalized standard deviation (%)
R^2	Determination (or regression) coefficient
SSE	Sum of square error
χ^2	Chi-square coefficient
y_c	Predicted data obtained from the model
y_e	Experimental data

Data availability

All data generated or analyzed during this study are included in this manuscript. The authors declare that they did not use databases or AI for the creation of the article.

Author contributions

Saeed Hassan Boroojerdi: conceptualization, investigation, writing – original draft, writing – review & editing. Mohsen

Mirmohammadi: project administration, data curation, methodology, resources, supervision. Farzad Bahadoran: project administration, data curation, methodology, resources, supervision.

Conflicts of interest

The authors declare that they have no known competing financial interests or personal relationships that could have appeared to influence the work reported in this article.

Acknowledgements

The authors extend their gratitude to the Research Institute of Petroleum Industry (particularly the Laboratory and Technical Services Department of the Gas Research Center and the Refining Research Center) for providing all the necessary facilities and equipment. They also express their appreciation to the expert and distinguished technical staff for their valuable insights throughout this research.

References

1 D. Safriet and E. I. Branch, *Locating and Estimating Air Emissions from Sources of Methylene Chloride, Final Report*, EPA, North Carolina, 1993.

2 D. A. Vallero, *Fundamentals of Air Pollution*, Academic Press, Elsevier, 5th edn, 2014.

3 IARC Working Group on the Evaluation of Carcinogenic Risks to Humans, *Re-evaluation of Some Organic Chemicals, Hydrazine and Hydrogen Peroxide*, International Agency for Research on Cancer, 1999.

4 F. Tian, X. Zhang and Y. Chen, *RSC Adv.*, 2016, **6**, 31214–31224, DOI: **10.1039/C5RA23888A**.

5 T. Salthammer, *Indoor Air*, 2016, **26**, 25–38, DOI: **10.1111/ina.12173**.

6 A. Lafond, *IAQ Standards and Guidelines (EPA and ASHRAE Standard)*, accessed 20, 2021.

7 R. Hossaini, M. Chipperfield, S. Montzka, A. Leeson, S. Dhomse and J. Pyle, *Nat. Commun.*, 2017, **8**, 15962, DOI: **10.1038/ncomms15962**.

8 B. Li, S. S. H. Ho, X. Li, L. Guo, A. Chen, L. Hu, Y. Yang, D. Chen, A. Lin and X. Fang, *Environ. Int.*, 2021, **156**, 106710, DOI: **10.1016/j.envint.2021.106710**.

9 P. Sakunkoo, S. Phonphinyo, N. Maneenin, C. Jirapornkul, Y. Limmongkon, J. Rayubkul, S. Thongtip and S. Sangkham, *Atmosphere*, 2021, **12**, 1694, DOI: **10.3390/atmos12121694**.

10 U. Ryu, S. Jee, P. C. Rao, J. Shin, C. Ko, M. Yoon, K. S. Park and K. M. Choi, *Coord. Chem. Rev.*, 2021, **426**, 213544, DOI: **10.1016/j.ccr.2020.213544**.

11 F. Tian, X. Zhang and Y. Chen, *RSC Adv.*, 2016, **6**, 63895–63904, DOI: **10.1039/c6ra07637h**.

12 N. El Messaoudi, D. S. P. Franco, S. Gubernat, J. Georgin, Z. M. Şenol, Z. Ciğeroğlu, D. Allouss and M. El Hajam, *Environ. Res.*, 2024, **252**, 118857, DOI: **10.1016/j.envres.2024.118857**.

13 H. Weldekidan, H. Patel, A. Mohanty and M. Misra, *Carbon Capture Sci. Technol.*, 2024, **10**, 100149, DOI: **10.1016/j.ccst.2023.100149**.

14 S. Wang, Y. Liu, C. Zhang, S. Guo and Y. Li, *Atmosphere*, 2024, **15**, 238, DOI: **10.3390/atmos15020238**.

15 X. Zhang, B. Gao, A. E. Creamer, C. Cao and Y. Li, *J. Hazard. Mater.*, 2017, **338**, 102–123, DOI: **10.1016/j.jhazmat.2017.05.013**.

16 W. K. Pui, R. Yusoff and M. K. Aroua, *Rev. Chem. Eng.*, 2019, **35**, 649–668, DOI: **10.1515/revce-2017-0057**.

17 X. Ma, L. Yang and H. Wu, *J. Cleaner Product.*, 2021, **302**, 126925, DOI: **10.1016/j.jclepro.2021.126925**.

18 X. Li, L. Zhang, Z. Yang, P. Wang, Y. Yan and J. Ran, *Sep. Purif. Technol.*, 2020, **235**, 116213, DOI: **10.1016/j.seppur.2019.116213**.

19 Z. Heidarinejad, M. H. Dehghani, M. Heidari, G. Javedan, I. Ali and M. Sillanpää, *Environ. Chem. Lett.*, 2020, **18**, 393–415, DOI: **10.1007/s10311-019-00955-0**.

20 A. Sandeep and A. Ravindra, *Diamond Relat. Mater.*, 2024, **146**, 111158.

21 Approved by the World Agricultural Outlook Board, Foreign Agricultural Service, *World Agricultural Production*, USA, 2023, p. 39.

22 *World Peanut Production by Country*, Altas Big, 2022, **https://www.atlasbig.com/en-us/countries-peanut-production**.

23 M.-A. Perea-Moreno, F. Manzano-Agugliaro, Q. Hernandez-Escobedo and A.-J. Perea-Moreno, *Sustainability*, 2018, **10**, 3254, DOI: **10.3390/su10093254**.

24 N. P. Gitama, N. Hidayat and D. Pebrianti, *Evrimata J. Mech. Eng.*, 2024, 88–96, DOI: **10.1016/j.jmrt.2020.03.041**.

25 J. Serafin and B. Dziejarski, *Environ. Sci. Pollut. Res.*, 2024, **31**, 40008–40062, DOI: **10.1007/s11356-023-28023-9**.

26 H.-C. Hsi, R. S. Horng, T.-A. Pan and S.-K. Lee, *J. Air Waste Manage. Assoc.*, 2011, **61**, 543–551, DOI: **10.3155/1047-3289.61.5.543**.

27 H. Cornell, M. Hayes, C. A. Hill and Associates and U. S. Environmental Protection Agency Technology Transfer, *Process Design Manual for Carbon Adsorption*, U.S. Environmental Protection Agency, Technology Transfer, 1973.

28 Y. Gao, Q. Yue, B. Gao and A. Li, *Sci. Total Environ.*, 2020, **746**, 141094, DOI: **10.1016/j.scitotenv.2020.141094**.

29 P. Li, K. Wan, H. Chen, F. Zheng, Z. Zhang, B. Niu, Y. Zhang and D. Long, *Catalysts*, 2022, **12**, 1067, DOI: **10.3390/catal12091067**.

30 M. J. Prauchner, K. Sapag and F. Rodríguez-Reinoso, *Carbon*, 2016, **110**, 138–147, DOI: **10.1016/j.carbon.2016.08.092**.

31 J. H. Lee, Y.-M. Kang and K. C. Roh, *Mater. Chem. Phys.*, 2024, **312**, 128587, DOI: **10.1016/j.matchemphys.2023.128587**.

32 L. S. Ribeiro and M. F. R. Pereira, *Sustainability*, 2024, **16**, 3038, DOI: **10.3390/su16073038**.

33 M. A. Al-Ghouti and D. A. Da'ana, *J. Hazard. Mater.*, 2020, **393**, 122383, DOI: **10.1016/j.jhazmat.2020.122383**.

34 S. Wang, H. Nam and H. Nam, *J. Environ. Chem. Eng.*, 2020, **8**, 103683, DOI: **10.1016/j.jece.2020.103683**.

35 G. Kumari, B. Soni and S. K. Karmee, *J. Inst. Eng.*, 2022, **103**, 15–22, DOI: **10.1007/s40034-020-00176-z**.

36 R. Malik, D. Ramteke and S. Wate, *Indian J. Chem. Technol.*, 2006, **13**, 319–328, http://nopr.niscpr.res.in/handle/123456789/7048.

37 A. H. Bedane, T. X. Guo, M. Eić and H. Xiao, *Can. J. Chem. Eng.*, 2019, **97**, 238–246, DOI: 10.1002/cjce.23330.

38 H. Shang, Y. Lu, F. Zhao, C. Chao, B. Zhang and H. Zhang, *RSC Adv.*, 2015, **5**, 75728–75734, DOI: 10.1039/C5RA12406A.

39 H. Wu, R. Chen, H. Du, J. Zhang, L. Shi, Y. Qin, L. Yue and J. Wang, *Adsorpt. Sci. Technol.*, 2019, **37**, 34–48, DOI: 10.1177/0263617418807856.

40 T. Tay, S. Ucar and S. Karagöz, *J. Hazard. Mater.*, 2009, **165**, 481–485, DOI: 10.1016/j.jhazmat.2008.10.011.

41 X. Wang, J. S. Lee, C. Tsouris, D. W. DePaoli and S. Dai, *J. Mater. Chem.*, 2010, **20**, 4602–4608, DOI: 10.1039/B925957K.

42 S. K. Theydan and M. J. Ahmed, *J. Anal. Appl. Pyrolysis*, 2012, **97**, 116–122, DOI: 10.1016/j.jaap.2012.05.008.

43 M.-b. Wu, R.-c. Li, X.-j. He, H.-b. Zhang, W.-b. Sui and M.-h. Tan, *New Carbon Mater.*, 2015, **30**, 86–91, DOI: 10.1016/S1872-5805(15)60178-0.

44 J. Fang, B. Gao, A. Mosa and L. Zhan, *Chem. Speciation Bioavailability*, 2017, **29**, 197–204, DOI: 10.1080/09542299.2017.1403294.

45 M. A. Franciski, E. C. Peres, M. Godinho, D. Perondi, E. L. Foletto, G. C. Collazzo and G. L. Dotto, *Waste Manage.*, 2018, **78**, 630–638, DOI: 10.1016/j.wasman.2018.06.040.

46 R. Nedjai, N. A. Kabbashi and M. Z. Alam, *J. Environ. Treat. Tech.*, 2021, **9**, 686–697, DOI: 10.47277/JETT/9(3)697.

47 A. F. Abbas and M. J. Ahmed, *J. Water Process Eng.*, 2016, **9**, 201–207, DOI: 10.1016/j.jwpe.2016.01.004.

48 H. B. Saeed, PhD thesis, Tehran University, 2023.

49 M. A. Mohamed, A. K. Galwey and S. A. Halawy, *Thermochim. Acta*, 2002, **387**, 63–74, DOI: 10.1016/S0040-6031(01)00830-9.

50 D. Adinata, W. M. A. Wan Daud and M. K. Aroua, *Bioresour. Technol.*, 2007, **98**, 145–149, DOI: 10.1016/j.biortech.2005.11.006.

51 K. Foo and B. Hameed, *Bioresour. Technol.*, 2012, **104**, 679–686, DOI: 10.1016/j.biortech.2011.10.005.

52 T. Horikawa, Y. Kitakaze, T. Sekida, J. i. Hayashi and M. Katoh, *Bioresour. Technol.*, 2010, **101**, 3964–3969, DOI: 10.1016/j.biortech.2010.01.032.

53 S. Habchi, N. Lahboubi, M. Asbik and H. El Bari, *Environ. Adv.*, 2024, **15**, 100477, DOI: 10.1016/j.envadv.2023.100477.

54 P. Ehiomogue, I. I. Ahuchaogu and I. E. Ahaneku, *Acta Tech. Corviniensis Bull. Eng.*, 2021, **14**, 87–96.

55 I. Langmuir, *J. Am. Chem. Soc.*, 1916, **38**, 2221–2295.

56 H. Freundlich, *Z. Phys. Chem.*, 1907, **57**, 385–470.

57 S. Lamidi, N. Olaleye, Y. Bankole, A. Obalola, E. Aribike and I. Adigun, *Applications of Response Surface Methodology (RSM) in Product Design, Development, and Process Optimization*, IntechOpen, 2022, DOI: 10.5772/intechopen.106763.

58 A. T. Abbas, A. E. Ragab, E. A. El-Danaf and E. A. Al Bahkali, *Proc. Inst. Mech. Eng., Part B*, 2018, **232**, 995–1006, DOI: 10.1177/0954405416662083.

59 R. Zafari, M. Abdouss and Y. Zamani, *Fuel*, 2019, **237**, 1262–1273, DOI: 10.1016/j.fuel.2018.10.074.

60 R. H. Myers, D. C. Montgomery and C. M. Anderson-Cook, *Response Surface Methodology: Process and Product Optimization Using Designed Experiments*, John Wiley & Sons, 2016.

61 F. Ghorbani, S. Kamari, S. Zamani, S. Akbari and M. Salehi, *Surf. Interfaces*, 2020, **18**, 100444, DOI: 10.1016/j.surfin.2020.100444.

62 C. J. Geankoplis, A. A. Hersel, D. H. Lepek, *Transport Processes and Separation Process Principles*, Prentice Hall Press, 5th edn, 2018.

63 S. Kamariya, J. Pandya and S. Charola, *Int. J. Trend Res. Dev.*, 2016, **3**, 138–141.

64 A. Fletcher, T. Somorin and O. Aladeokin, *BioEnergy Res.*, 2024, **17**, 467–478, DOI: 10.1007/s12155-023-10683-7.

65 J. Rouquerol, F. Rouquerol, P. Llewellyn, G. Maurin and K. Sing, *Adsorption by Powders and Porous Solids: Principles, Methodology and Applications*, Academic press, 2013.

66 R. C. Bansal and M. Goyal, *Activated Carbon Adsorption*, CRC press, Taylor & Francis Group, 2005.

67 Y.-D. Chen, W.-Q. Chen, B. Huang and M.-J. Huang, *Chem. Eng. Res. Des.*, 2013, **91**, 1783–1789, DOI: 10.1016/j.cherd.2013.02.024.

68 W. Shen, Z. Li and Y. Liu, *Recent Pat. Chem. Eng.*, 2008, **1**, 27–40, DOI: 10.2174/2211334710801010027.

69 O. A. Hussain, A. S. Hathout, Y. E. Abdel-Mobdy, M. Rashed, E. A. Rahim and A. Fouzy, *Toxicol. Rep.*, 2023, **10**, 146–154.

70 M. S. Shafeeyan, W. M. A. W. Daud, A. Houshmand and A. Shamiri, *J. Anal. Appl. Pyrolysis*, 2010, **89**, 143–151, DOI: 10.1016/j.jaap.2010.07.006.

71 B. M. V. D. Gama, C. M. B. de Menezes Barbosa, J. M. Rodriguez-Diaz, D. C. S. Sales and M. M. M. B. Duarte, *Chem. Eng. Commun.*, 2022, **209**, 736–756, DOI: 10.1080/00986445.2021.1903885.

72 A. L. Cazetta, A. M. Vargas, E. M. Nogami, M. H. Kunita, M. R. Guilherme, A. C. Martins, T. L. Silva, J. C. Moraes and V. C. Almeida, *Chem. Eng. J.*, 2011, **174**, 117–125, DOI: 10.1016/j.cej.2011.08.058.

73 K. Foo and B. Hameed, *Bioresour. Technol.*, 2012, **103**, 398–404, DOI: 10.1016/j.biortech.2011.09.116.

74 M. Banerjee, R. K. Basu and S. K. Das, *Environ. Sci. Pollut. Res.*, 2019, **26**, 11542–11557, DOI: 10.1007/s11356-018-1930-5.

75 L. Li, S. Liu and J. Liu, *J. Hazard. Mater.*, 2011, **192**, 683–690, DOI: 10.1016/j.jhazmat.2011.05.069.

76 S. Kang, J. Ma, Q. Wu and H. Deng, *J. Chem. Eng. Data*, 2018, **63**, 2211–2218, DOI: 10.1021/acs.jced.8b00174.

77 C. Borkar, D. Tomar and S. Gumma, *J. Chem. Eng. Data*, 2010, **55**, 1640–1644, DOI: 10.1021/je900706h.

78 N. Qiang, T. Shi, T. Liu, Y. Cao, H. Miu and J. He, *IOP Conference Series: Earth and Environmental Science*, IOP Publishing, 2019, DOI: 10.1088/1755-1315/295/2/012033.

79 Y. Zhou, L. Zhou, X. Zhang and Y. Chen, *Microporous Mesoporous Mater.*, 2016, **225**, 488–493, DOI: 10.1016/j.micromeso.2016.01.047.

80 S.-H. Jung and J.-S. Kim, *J. Anal. Appl. Pyrolysis*, 2014, **107**, 116–122, DOI: 10.1016/j.jaap.2014.02.011.

81 M. Moheb, A. M. El-Wakil and F. S. Awad, *RSC Adv.*, 2025, **15**, 674–687, DOI: 10.1039/d4ra07957d.

82 M. Ahmed and T. Kuwabara, *Toxics*, 2024, **12**, 280, DOI: 10.3390/toxics12040280.

83 K. Y. Foo and B. H. Hameed, *Chem. Eng. J.*, 2010, **156**, 2–10, DOI: 10.1016/j.cej.2009.09.013.

84 G. J. Amrutha, C. Girish, B. Prabhu and K. Mayer, *Environ. Processes*, 2023, **10**, 38, DOI: 10.1007/s40710-023-00631-0.

85 J. Park, J. D. Howe and D. S. Sholl, *Chem. Mater.*, 2017, **29**, 10487–10495, DOI: 10.1021/acs.chemmater.7b04287.

86 S. Lagergren, Kungliga svenska vetenskapsakademiens, *Handlingar*, 1898, **24**, 1–39.

87 G. Blanchard, M. Maunaye and G. Martin, *Water Res.*, 1984, **18**, 1501–1507.

88 J. O. Ighalo, F. O. Omoarukhe, V. E. Ojukwu, K. O. Iwuozor and C. A. Igwegbe, *Cleaner Chem. Eng.*, 2022, **3**, 100042, DOI: 10.1016/j.clce.2022.100042.

89 *Potassium Oxalate Factory Supply 99% Min Good Price* $K_2C_2O_4$ H_2O *583-52-8 Potassium Oxalate*, 2024, https://fengdachem.en.made-in-china.com/product/bdhtVzglgYUu/China-Potassium-Oxalate-Factory-Supply-99-Min-Good-Price-K2c2o4-H2O-583-52-8-Potassium-Oxalate.html.

90 *World's lowest electricity prices found in Iran and Syria*, 2023, https://tribune.com.pk/story/2491956/worlds-lowest-electricity-prices-found-in-iran-and-syria#google_vignette.

91 G. Selvaraju and N. K. A. Bakar, *J. Cleaner Product.*, 2017, **141**, 989–999, DOI: 10.1016/j.jclepro.2016.09.056.

92 IndexBox, *Activated Carbon Price in United States Hits New Record of $6,401 per Ton*, 2023, https://www.globaltrademag.com/activated-carbon-price-in-united-states-hits-new-record-of-6401-per-ton/.